The measurement and impact of negative oxygen ions during reactive sputter deposition

D. Depla

Department of Solid State Sciences, Ghent University, Krijglaan 281 (S1), 9000 Gent, Belgium

ARTICLE HISTORY
Compiled September 27, 2023

ABSTRACT
Many thin film applications are based on oxides. The optimization of the oxide properties is an on-going process and requires a deep understanding of the deposition process. A typical feature of reactive (magnetron) sputter deposition is the presence of negative oxygen ions. Two groups of ions can be identified based on their energy. Low energy ions are generated in the bulk of the discharge. The high energy ions are emitted from the oxide or oxidized target surface. As these ions are generated at the cathode, they are accelerated by the electric field towards the growing film. Depending on the discharge voltage and the powering method, their energy is typically several tenths to hundreds electron volt. As such the ions can have a strong impact on the film properties. In the case of magnetron sputtering, this will lead to inhomogenous film properties over the substrate facing the locally eroded target. Due to their high energy, the trajectory of negative ions can be easily predicted which has led to several strategies to avoid negative ion bombardment such as facing target sputtering and off-axis sputtering. This paper reviews several facets of the production, the measurements and the impact on the film properties of negative ions during reactive sputtering. Despite the many illustrative studies on the impact of negative oxygen ions, quantification is often lacking as the negative ion yield is only known for a few oxides. The compilation of several literature sources allows the discussed trends to be placed in a quantitative framework.

KEYWORDS
negative ion yield; magnetron sputtering; ion assisted deposition

1. Introduction

The presence of negative ions in gas discharges was already postulated in the very first paper on sputtering. Indeed, the paper by Grove, identified as the first paper on sputtering [1], states: "*My present experiments show, I believe, that in induction across gaseous dielectrics there is a commencement, so to speak, of decomposition, a polar arrangement not merely of the molecules, irrespective of their chemical characters, but a chemical alternation of their forces, the electronegative element being determined or directed, though not traveling in one direction, and the electropositive in the opposite direction.*" [2].

Although the observation of negative oxygen emission from surfaces bombarded with positive ions was already reported earlier [3, 4], the research on their impact during

CONTACT D. Depla Email: `Diederik.Depla@ugent.be`,

sputtering of oxides took really off by a prediction based on a study of the etching of the deposit by negative Au^- ions from rare-earth/gold targets [5, 6]. The occurrence of etching of the deposit could be related to the difference between the electron affinity of Au and the ionization energy of the rare-earth. In this way, a measure of the energy required to transfer an electron from the first constituent element of the target compound to the second element was obtained. Based on the data at hand, an upper threshold value of 3.4 eV was suggested to observe etching. The papers state that this indicates that film growth of several oxides (and other compounds) could be influenced by negative ion bombardment. The authors realized that the negative ion production will probably not be characterized by the calculated hard threshold. Indeed, it was shown later that the occurrence of negative ion etching of several oxides was observed for higher values than the aforementioned difference [7]. It should be mentioned that the evaluation in both cases is based on the deposition/etch rate and not on the probability of negative ion emission. The etching will not only be defined by the ability to emit negative ions from the target, but also by the energy of the negative species, and the sputtering yield of the deposit by these ions. The connection between the straightforward observation of etching and a quantitative threshold however was a motivation for many to investigate the importance of negative oxygen ion (NOI) bombardment.

This paper reviews the current knowledge of NOI bombardment during sputter deposition. The paper is organized as follows. First, the measurement of NOI during (magnetron) sputtering will be highlighted. Secondly, the production of NOIs in the discharge bulk and at the cathode will be discussed. Based on the current knowledge, the NOI yield will be quantified. Some methods to avoid NOI bombardment will be treated after modeling of the ion trajectories. In a final section, the effect of NOI during film growth is reviewed. The knowledge on NOIs will be briefly confronted with the observation of other negative ions during sputter deposition.

2. Measurement of negative oxygen

2.1. *Mass spectrometry*

NOIs can together with other ions be easily detected by mass spectrometry during reactive sputtering. Important for the interpretation of the observed results is that the mass spectrometer has typically a low acceptance angle which is energy dependent. A power law dependence of the acceptance angle A on the ion energy E has been reported:

$$A \propto E^{-n} \tag{1}$$

with several values for n (0.3 [8],1.61 [9]). The acceptance angle is as low as a few degrees for ion energies larger than 100 eV. High energy ions will only be measured when traveling almost perpendicular towards the mass spectrometer orifice due to the low acceptance angle. Ions released from inclined or tilted surfaces, will not be measured although they can still affect the film growth. This topic will be further discussed in section 6 but can already be illustrated by one example. No high energy NOIs were measured with mass spectrometry during the sputter deposition of Ti-Cr-oxides, in contrast to other reports for similar materials [10, 11]. The reason is the specific used geometry, i.e. magnetron assemblies in a dual magnetron configuration tilted versus the mass spectrometer axis.

A second concern regarding mass spectrometry is that the technique as used during

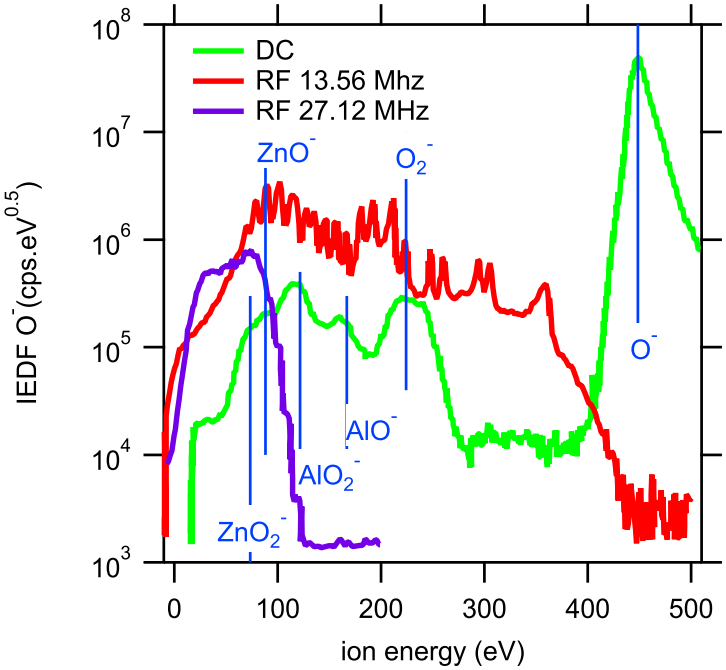

Figure 1. Ion energy distribution functions (IEDF) of O^- measured during DC and RF sputtering of an Al doped ZnO (AZO) target. The discharge power was 50 W and the argon pressure was 0.5 Pa during all experiments. The blue lines are the expected energies based on the dissociation of complex ions accelerated to the discharge voltage. The label indicates the mother ion. The energy has been calculated by a multiplication of the energy defined by the discharge voltage (peak at O^-) with the ratio of the atomic mass of oxygen and the mass of the mother ion (see also Equation 3). Data taken from Welzel and Ellmer [13].

sputter deposition doesn't provide quantitative data. The NOI count rate can only be compared in a relative way and the NOI yield cannot be quantified.

Not only the presence of negative ions can be evaluated, but more advanced mass spectrometers permit the measurement of their energy distribution. (Magnetron) gas discharges can be powered in different ways known as radio-frequency (RF), direct current (DC), pulsed DC and high power impulse magnetron sputtering (HiPIMS). The powering method affects the energy distribution observed (Figure 1). Ishibashi and co-workers [12] have studied the oxygen energy distribution for five different materials (indium tin oxide, ZnO, barium copper oxide, yttrium barium oxide, and lead zirconium titanate) at constant discharge power for both RF and DC magnetron discharges. The authors observe that the energy distribution for DC discharges shows typically one major peak at an energy defined by the discharge voltage together with some minor peaks at lower energies [14]. Two dimensional particle-in-cell/Monte Carlo simulations show a similar result [15]. In contrast the energy distribution as measured during RF powering is much more complicated which is confirmed by other research groups [16, 13].

In a DC magnetron discharge almost the entire applied voltage between cathode and anode falls across the cathode sheath [17]. Negative ions released from the cathode/target will therefore have an energy comparable to the value of the applied voltage (Figure 1). Strictly speaking, the ions are accelerated between the cathode and the plasma potential. The ion energy is however measured versus ground potential, and hence the registered energy is defined by the discharge voltage only. As the discharge voltage can be tuned by different deposition parameters, it is possible to change the negative ion energy by the magnetic field strength [18, 19, 20], the discharge pressure

[14, 20], the discharge current/power [14, 20], and the sputter gas composition [14, 20].

There is no low energy tail of the high energy NOI peak which indicates that no negative ion formation occurs in the sheath itself [21]. The high energy tail of the peaks can be explained from the energy distribution for sputtered atoms which typically follows a Thompson distribution. At low energy the distribution is described by [22]

$$f\left(E\right) \propto \frac{E}{\left(E+U_{\mathrm{s}}\right)^{3}} \tag{2}$$

where U_s is the surface binding energy of the sputtered species. The restricted knowledge regarding the surface binding energy of oxygen hinders accurate fitting. From the several approaches to determine the surface binding energy, one can indeed learn that the surface binding energy for oxygen is rather unknown, or at least only very approximate. Ta_2O_5 is a well characterized material as it is used as a calibration standard during XPS depth profiling [23], but even for this material strongly different surface binding energy values can be found: an analytical model gives a value of 7.93 eV [24], a thermodyamic based calculation 2.61 eV [25], the suggested input for the Monte Carlo package TRIDYN is 6.7 eV [26], for another Monte Carlo package SRIM 2 eV [27], while experimental data gives a surface binding energy of 4.7 eV [28]. Further, the correctness of the energy distribution at low energy is debated [29, 30].

Mass spectrometry shows also the ejection of negative clusters which are accelerated over the cathode sheath [31, 32, 33]. The dissociation due to impact with the sputter gas results in the formation of smaller clusters and NOIs. This process explains the presence of other lower energy peaks in the energy spectrum [34, 35, 19, 32]. The peak position can be calculated based on energy and momentum conservation,

$$E_{\mathrm{c}} = \frac{M_{\mathrm{c}}}{M_{\mathrm{m}}} E_{\mathrm{m}} \tag{3}$$

where E is the ion energy and M the ion mass for the child (c) and mother (m) ion. The energy lost during the collision is small and neglected in the calculation. The calculated energy of NOIs that originate from different mother ions is demonstrated in Figure 1 (blue lines).

Low energy NOIs can also be present in the gas discharge. The origin of these ions will be discussed in section 3. These are not observed in Figure 1, but in many other studies the energy spectrum shows an intense low energy peak attributed to these bulk NOIs entering the mass spectrometer [33, 36]. The difference depends on the electrical configuration of the mass spectrometer orifice. When the orifice is at floating potential V_{f}, ions with an energy lower than eV_{f} cannot enter the mass spectrometer. The floating potential however does not shift the energy distribution because this potential barrier is only passed leading to a deceleration and acceleration before and after the orifice, respectively. The deposition of isolating films can change the potential from grounded to floating.

Based on the information that the negative ions (and clusters) are sputtered, the energy distribution of the negative ions measured during DC powering [35, 36] has been modeled based on the Thompson distribution (Equation 2),

$$f\left(E\right) \sim e \int_{E_{\mathrm{min}}}^{E} g\left(V_{\mathrm{d}}\right) \times \frac{E - eV_{\mathrm{d}}}{\left[\left(E - eV_{\mathrm{d}}\right) + U_{\mathrm{s}}\right]^{3}} dV_{\mathrm{d}} \tag{4}$$

where V_{d} is the discharge voltage, E_{min} is the energy which corresponds to the minimal measured absolute voltage of the discharge voltage. The function $g\left(V_d\right)$ accounts the variation of the DC discharge voltage which have shown to be a Gaussian with a mean discharge voltage and a given standard deviation.

Similar results as for DC sputtering have been obtained for pulsed DC experiments [37, 36]. During pulsed DC powering, the discharge voltage is time dependent. This requires to change the latter equation to [36],

$$f\left(E\right) \sim \int\limits_{pulse} g\left(t\right) \times \frac{E - eV_{\mathrm{d}}\left(t\right)}{\left[\left(E - eV_{\mathrm{d}}\left(t\right)\right) + U_{\mathrm{s}}\right]^3} dt$$
$$\text{where} \tag{5}$$
$$g\left(t\right) = \begin{cases} 1 \text{ for } eV_{\mathrm{d}}\left(t\right) \leq E \\ 0 \text{ for } eV_d\left(t\right) > E \end{cases}$$

The integration is carried out over the pulse.

The ion energy distribution function is much broader for the RF discharges (Figure 1). The broadening is caused by the oscillation of the target potential around the self-bias potential. As the ion ejection mechanism is expected to be the same as during DC sputtering, the obtained spectrum is the result of overlapping spectra for each momentary potential. The peaks within the broad distribution are no artifacts but real structures from the discharge, confirmed by measurements by other research teams [38, 39, 40]. The kinetic energy of the ions before entering the mass spectrometer is defined by the oscillating target and plasma potential. In contrast to DC sputtering, the ions have therefore different energy and hence a different transit time to reach the mass spectrometer. The plasma potential at the time of arrival at the mass spectrometer orifice is different, and will be function of the initial kinetic energy as the latter defines the time of arrival. This results in a modulation of the detected ion energy, and explains the presence of the peaks within the broad energy distribution. A similar effect have been described for pulsed DC where two peaks are observed: one for ions that reach the mass spectrometer during the pulse, and those arriving during the off-period [41]. A combination of both types of distributions can be obtained [42] by mixing RF and DC powering. This mixing also allows the target DC bias to be modified, and hence to influence the negative ion energy [43]. The latter will be discussed in more detail further in the paper.

2.2. *Current measurements*

Negative ions are charged species and hence it is possible to detect them by measuring their current. Other species are deflected from the current collector by the application of electric and magnetic fields. As the negative ions can generated secondary electrons on their impact at the current collector, it is necessary to design the probe in such way that these secondary electrons are not detected.

One of the first, and often cited, papers on NOI bombardment during RF magnetron sputtering of $YBa_2Cu_3O_{7\text{-}x}$ (YBCO) superconductors discusses how this technique can be used to explain the loss in deposition rate and the preferential sputtering of Ba and Cu due to NOI bombardment at the substrate [44]. The method was used to calculate the negative ion yield using some assumptions. Especially, the assumption of equal secondary electron yield from the collecting electrode by positive ion bombardment and

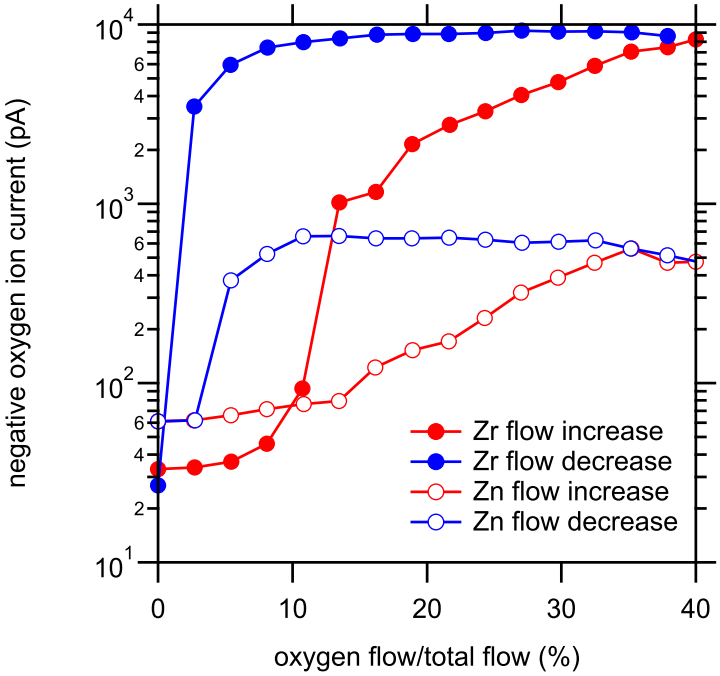

Figure 2. The negative oxygen ion current as function of the oxygen-to-total flow ratio during reactive magnetron sputtering of Zn and Zr. The negative ion current was attributed to negative ions based on experiments with a more advanced time-of-flight set-up. Experiments were performed at constant discharge current (80 mA) and total pressure (0.67 Pa). Data taken from Tominaga and Kikuma [46].

fast neutrals seems to make the estimated negative ion yield questionable. The method is however also used during ion beam sputtering. Due to the inclination of the ion beam with the target, the signal towards the current sensor will be less affected by high energetic argon neutrals, and hence the reported values (0.5±0.1 and 0.3±0.1 for the electron and negative ion yield, respectively) can be trusted. The emission of negative ions species from YBCO was also studied at low Ar^+ ion energies using secondary ion mass spectrometry (SIMS). It is confirmed that the highest contribution corresponds to $O^-(OH^-)$ ions which exceeds by far the yield of other secondary negative ions. The addition of oxygen during the argon bombardment enhances further the negative ion yield [45]. A similar approach was demonstrated for magnetron and diode sputtering of ZnO (and $BaTiO_3$) [47, 48]. The authors could proof that only high energetic oxygen ions were entering the probe by using a time-of-flight set-up. By measuring also the emitted secondary electrons from the CuBe current collector, they were able to detect high energetic oxygen neutrals. The latter signal contains also a contribution of emitted photons from the gas discharge which could be eliminated by its pressure independency. The collected negative ion current strongly decreases with increasing pressure which is explained from gas scattering, neutralization and electron detachment. The authors studied the negative oxygen emission for both Zn and Zr sputtered reactively in an argon-oxygen mixture in a follow-up study [46]. Measurements are performed as a function of the oxygen-to-total flow ratio. Figure 2 shows that the collected negative oxygen ion current shows hysteresis typically for reactive magnetron sputtering experiments [49]. This indicates that the negative ion emission is much more important when the target is poisoned. The poisoned state of the target was confirmed by measurements of the deposition rate based on the photoemission of Zn and Zr lines, and the discharge voltage behavior. Similar trends in the hysteresis behavior as for other process parame-

ters is demonstrated for Zr/O_2 reactive sputtering [50] and Ti/O_2 [51]. Comparison of the three studied materials under the same conditions (80 mA, total pressure 0.67 Pa, 80%/20% argon/oxygen) the negative ion current decreases from Zr, over Zn to Ti. Also other studies confirm the requirement to have a (partially) oxidized target surface to observe negative oxygen emission [52].

A technique, similar to other aforementioned methods, is known as magnetic filtering probe measurements. The probe is principally based on a series of grid electrodes in conjunction with a magnetic filter. The transverse magnetic field, arranged perpendicularly to the particle flux direction, filters the plasma electrons from the bombarding flux by magnetizing them. The potential on the electrodes hinders positive ions to be measured and hence only negative ions reach the detector. The technique has been used to measure the negative ion flux during reactive sputtering of Ti in an oxygen/argon mixture [53]. The authors report a negative ion yield of approximately 1.1×10^{-3} for a poisoned Ti target.

2.3. *Energy flux measurements*

The high energy of the NOIs ejected from the target can be measured with an energy flux probe. Together with several other species, negative ions contribute to the energy flux. To distinguish among these species additional diagnostics and/or modeling is required. Moreover, not all energy of the impinging negative ions is transferred into heat. Energy losses through electron detachment, secondary electron emission, backscattering, and re-sputtering could affect the measurements. Calculations performed in the context of energy flux measurements during indium tin oxide (ITO) depositions showed that the energy losses count for approximately 10% [54]. Target erosion can affect also the measured energy flux as the trajectory of high energetic negative ions is more directional as compared to sputtered and reflected atoms (see subsection 6.1). Hence, it is possible that the energy flux in poisoned mode, i.e. with a strong contribution of negative oxygen ions, is lower than in metallic mode [55]. Nevertheless, during reactive sputtering of CeO_2 [56, 57] and MgO [58] the energy flux was much larger as compared to the metallic mode, but also strongly dependent on the target erosion. Using modeling to account for space charge effects, it was possible to derive from the energy flux measurements for CeO_2 a negative ion yield of 0.015. A value of 3.3×10^{-3} was reported for ITO [54].

2.4. *Photodetachment measurements*

An electron from a negative charged oxygen ion can be detached by the impact of a photon with sufficient energy. This changes the discharge characteristics which can be probed from the optogalvanic signal generated by released electrons. The signal can be picked up either by the anode or by a probe [59]. The latter is also known as probe assisted laser optogalvanic spectroscopy [60]. As the electron removal increases the local electron density, it is also possible to use a Langmuir probe. The technique is known as Langmuir probe laser photodetachment. As it is necessary to avoid photo-stimulated electron emission from the Langmuir probe itself during the measurement, the probe is shielded by a carefully placed wire. This explains the alternative name for this technique, i.e. eclipse photodetachment.

The technique doesn't discriminate between the aforementioned groups of low, medium and high energy negative ions. It is possible to distinct between target-borne high energy oxygen ions and bulk negative oxygen during pulsed DC sputtering exper-

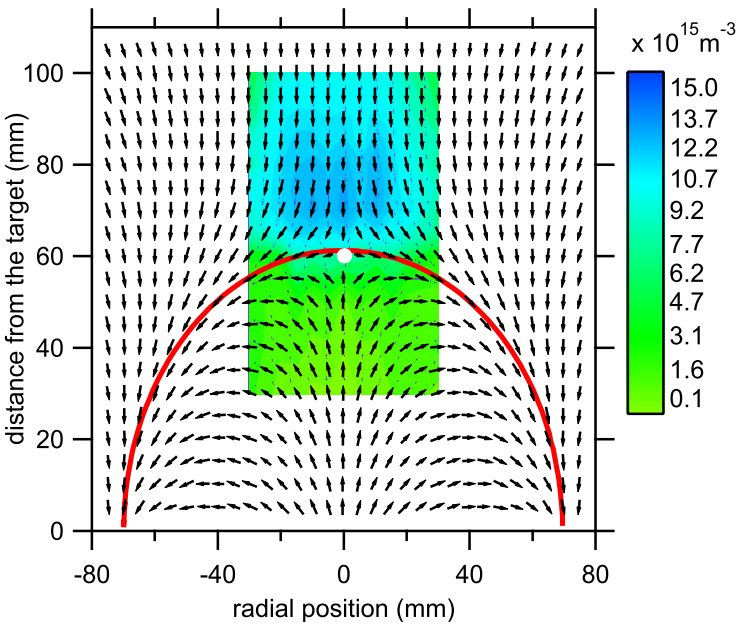

Figure 3. The NOI bulk density during reactive sputtering with a planar circular magnetron. Target material; Ti, total pressure: 2.4 Pa (0.48 Pa O_2), discharge power: 200 W. The discharge was in full poisoned mode. The magnetic field vectors (without magnitudes) are shown, together with a line representing the last closed flux surface separating the magnetic trap from the open plasma. The white dot represents the magnetic null. Data taken from Scribbins et al. [66](oxygen density) and from Dodd et al. [61] (magnetic field vectors).

iments by measurement of the negative oxygen ion density during the negative voltage pulse on the cathode (on phase) and after the negative pulse (off phase) [61]. This kind of experiments shows that the measured oxygen density is mainly dominated by low energetic negative ions for which, in contrast to the high energetic species, the negative ion density has a clear dependence on the position relative to the target as shown in Figure 3. The negative oxygen ions are mainly present in the high potential regions of the plasma above the closed field region of the magnetic trap and confined to an annulus-shaped region around the central axis. At the high pressure, i.e. 2.4 Pa as shown in Figure 3, the peak oxygen density is approximately twice the electron density. Measurements have also been performed at lower pressure which makes it possible to conclude that the area of the highest oxygen densities spreads out with increasing pressure, until NOIs start to occupy the central magnetic field-free region on the center line above the cathode target and to enter the top of the magnetic trap. The method has been employed during reactive magnetron sputtering of TiO_2 using DC [62], pulsed DC [61, 63, 64] and HiPIMS [65]. An alternative to measure the increased electron density by laser photodetachment is the usage of a resonant hairpin probe. The principle of the technique is based on the measurement of the plasma dielectric constant using a microwave resonant structure. When the resonator is placed in the plasma, the resonant frequency shift from its characteristic resonance frequency in vacuum. The electron density can be determined by this frequency shift. The simplest microwave resonator probe is a quarter-wavelength parallel transmission line, which has one end short-circuited and the other end open; therefore it resembles a hairpin. The main advantage of this technique is that the probe is floating and it requires no current collection to determine the density [67]. The bulk density of negative oxygen ions was measured during pulsed DC reactive sputtering using both Langmuir and resonant hairpin probe. The measurements shows that the negative ion density increases in the afterglow of the discharge

[68]. In the afterglow the electron temperature decreases, and therefore more negative ions can be formed as compared to the on-period of the pulse because the cross section for negative ion formation by dissociative attachment to excited oxygen molecules (see further, Figure 4) increases with decreasing electron energy.

Pure Langmuir probe measurements have also been employed. The main challenge is that some complex adjustments need to made to the developed theories for electropostive discharges [69, 70]. Hence, the results are based on the interpretation of the probe characteristics by a given theory. Often the plasma is complex and contains ions with different masses. The typical ion mass, required for the analysis of the ion flux towards the probe is not known in detail and is an aggregate of smaller molecular fragments. Langmuir probe measurements have been used to measure the behavior of negative oxygen ions in the afterglow of a reactive HiPIMS discharge [71]. The O^- concentration was found to decay more slowly as compared to the electron density which results in long-lived highly electronegative afterglow plasma's.

For sake of completeness, acoustic ion waves to probe magnetron discharges can also be used to measure negative ion concentrations [72].

3. Negative oxygen production in the discharge bulk

The description of the production of negative ions in the bulk of the gas discharge is important because their presence can alter the discharge operation. For example, the presence of negative ions in the discharge can significantly influence the positive ion flux impinging upon plasma-facing surfaces [73, 71]. Essential issues are the mechanisms of the negative ion generation and destruction, the influence of negative ions on transport properties of charged species (ambipolar diffusion), the structure of the plasma sheath (Bohm velocity), and finally the chemical interactions between neutrals and negative ions [74]. These topics have been investigated in the context of the usage of electronegative gases in the technology of plasma–surface processing, and the production of negative ion beams [75]. Some of the most important topics will be discussed in this section.

The density of negative ions in the bulk of the discharge during reactive (magnetron) sputtering is defined by several creation and destruction processes [76, 77, 78].

The formation of negative ions in low pressure discharges, where three body processes are not very plausible, is partially due to dissociative electron attachment to oxygen molecules and ion pair formation:

$$O_2 + e^- \rightarrow O + O^- \tag{6a}$$

$$O_2 + e^- \rightarrow O^+ + O^- + e^- \tag{6b}$$

The total cross section for negative ion formation has been studied by several researchers but the cross section reported by Rapp and Briglia [79] have been accepted as recommended data [80]. The cross section shows a broad peak (Figure 4) which is associated to Equation 6a by following resonance process [81]

$$e + O_2\left(X^3\Sigma_g^-\right) \rightarrow O_2^-\left(^2\Pi_u\right) \rightarrow O^-\left(^2P\right) + O\left(^3P\right) \tag{7}$$

At collision energies larger than 17 eV the production occurs through the ion pair mechanism (Equation 6b). The above dissociative attachment process is accepted as the major formation mechanism of negative ions in low-pressure plasmas. Dissociative

attachment may be strongly enhanced by vibrational/electronic excitation of the parent gas. Therefore, the production through metastable oxygen molecules has shown to be important [77]

$$\mathrm{O_2}\left(\mathrm{a^1\Delta_g}\right) + \mathrm{e^-} \rightarrow \mathrm{O^-} + \mathrm{O}\left(\mathrm{^3P}\right) \tag{8a}$$

$$\mathrm{O_2}\left(\mathrm{a^1\Delta_g}\right) + \mathrm{e^-} \rightarrow \mathrm{O^-} + \mathrm{O}\left(\mathrm{^1D}\right) \tag{8b}$$

$$\mathrm{O_2}\left(\mathrm{A^3\Sigma_u^+, A^3\Delta_u, c^1\Sigma_u}\right) + \mathrm{e^-} \rightarrow \mathrm{O^-} + \mathrm{O}\left(\mathrm{^3P}\right) \tag{8c}$$

$$\mathrm{O_2}\left(\mathrm{b^1\Sigma_g^+}\right) \rightarrow \mathrm{O} + \mathrm{O^-} \tag{8d}$$

The cross sections for these production mechanisms are also depicted in Figure 4. However, the impact of the latter reactions will depend on the electron temperature as the decay of a metastable oxygen molecule into pairs of neutral oxygen atoms can be far more dominant than the creation of metastable molecules.

The aforementioned formation processes are compensated by several destruction processes. Reported reactions with electrons are [82, 77]

$$\mathrm{e^-} + \mathrm{O^-} \rightarrow \mathrm{O} + \mathrm{e^-} + \mathrm{e^-} \tag{9}$$

Reported reactions with other species are [82, 83, 77]

$$\mathrm{O_2^+} + \mathrm{O^-} \rightarrow \mathrm{O_2} + \mathrm{O} \tag{10a}$$

$$\mathrm{O^+} + \mathrm{O^-} \rightarrow \mathrm{O} + \mathrm{O} \tag{10b}$$

$$\mathrm{O} + \mathrm{O^-} \rightarrow \mathrm{O_2} + \mathrm{e^-} \tag{10c}$$

$$\mathrm{O_2^+} + \mathrm{O^-} \rightarrow \mathrm{O} + \mathrm{O} + \mathrm{O} \tag{10d}$$

$$\mathrm{O_2} + \mathrm{O^-} \rightarrow \mathrm{O_3} + \mathrm{e^-} \tag{10e}$$

$$\mathrm{O^-} + \mathrm{O_2}\left(\mathrm{a^1\Delta_g}\right) \rightarrow \mathrm{O_3} + \mathrm{e^-} \tag{10f}$$

$$\mathrm{O^-} + \mathrm{O_2}\left(\mathrm{a^1\Delta_g}\right) \rightarrow \mathrm{O} + \mathrm{O_2^-} \tag{10g}$$

$$\mathrm{O^-} + \mathrm{O_2}\left(\mathrm{b^1\Sigma_g^+}\right) \rightarrow \mathrm{O_2} + \mathrm{O} + \mathrm{e^-} \tag{10h}$$

$$\mathrm{O^-} + \mathrm{Ar^+} \rightarrow \mathrm{O} + \mathrm{Ar} \tag{10i}$$

The formation and destruction of NOIs based on the aforementioned reactions was numerically studied, among other species, using a global volume averaged discharge model of an inductive coupled gas discharge as a function of the oxygen content in the gas discharge [77]. The major conclusions were that negative oxygen ions are produced by dissociative attachment to oxygen molecules with a strong contribution by dissociative attachment to metastable oxygen molecules (Equation 8). Negative oxygen ions are, at high argon content, mainly lost through interaction with positive argon ions (Equation 10i) and electrons (Equation 9). Similar results were obtained based on a hybrid Monte Carlo fluid model of a O_2/Ar DC discharges with low oxygen content (<5% oxygen) [78]. The latter simulations show a low bulk density for NOIs as compared to the electron density. One refers to the ratio of both densities as the electronegativity of the gas discharge which can, based on the simulation results, be calculated as approximately 5×10^{-5} for the lowest oxygen concentration (0.5%) up to 5×10^{-3} for the highest concentration (5%). At similar oxygen concentrations higher values were

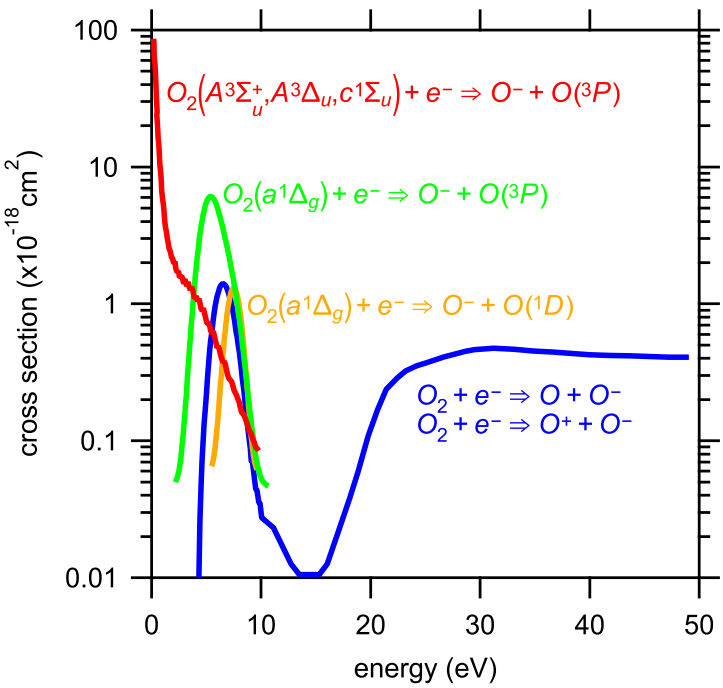

Figure 4. Cross section for several electron/oxygen interaction which lead to formation of NOIs. The blue corresponds with Equation 6 [79]. The green, orange and red curves corresponds to Equation 8a [84, 85],8b [84, 85], and 8c [86], respectively.

obtained for the aforementioned study of an inductive coupled gas discharge [77]. The latter study shows also an almost linear increase of the electronegativity as a function of the oxygen concentration within the discharge. The electronegativity reaches a value of 0.4 for a pure 500 W oxygen discharge. The authors report that the results are consistent with some experimental studies. Simulations have also been performed for magnetron discharges. A study on a DC magnetron discharge using a chromium target by a collisional–radiative model reports on an electronegativity of approximately 0.015, independently of the oxygen content in the discharge [87]. A PIC/MC simulation shows also very low electronegativity values, i.e. approximately 4×10^{-3} for 30% oxygen in the gas discharge [88]. The calculations are performed above the racetrack region. Another PIC/MC shows at similar oxygen content in the discharge an electronegativity value of 0.04 [89]. According both to PIC/MC simulations, a higher negative ion density is found further away from the cathode. This behavior is attributed to the difference in mass between electrons and negative ions [89]. The negative ions are generated in an area close to the cathode but in contrast to the electrons the heavy O^- ions are not trapped by the magnetic field. Therefore the negative ions will move towards the positive plasma potential region. A similar reasoning was used to explain the high electronegativity values experimentally measured in a region above the center of the target (Figure 3) [66].

To explain the observed difference between experimental and simulated NOI densities in pure oxygen DC discharges at pressures between 5 and 20 Pa, an alternative mechanism was suggested where oxygen ions are formed close to the cathode surface [74]. The authors propose that their formation is due to the interaction with high energy positive ions accelerated towards the cathode and oxygen molecules

$$\mathrm{O_2 + X^+\,(high\ E) \rightarrow O^+ + O^- + X^+} \tag{11}$$

Although this mechanism takes place close to the cathode, the negative ions are not produced at the cathode surface as will be discussed in the next section.

4. Negative oxygen production at the target surface

Negative ions can be formed at a surface based on two mechanisms [90]. Atoms or molecules that impinge on a hot surface can be ionized when re-evaporated. This mechanism, known as thermodynamic-equilibrium surface ionization, is perhaps only important during hot target sputter deposition, but will be less common during a more traditional usage of sputter deposition. The second mechanism is negative ion sputtering. An extensive amount of research have been performed to unravel this process of atomic secondary ion emission. There are two main driving forces for this research. First, negative ion emission is often observed and studied during SIMS.

A second motivation is the production of negative ion sources. As will be discussed further in the text, negative ions are often seen as a main disadvantage during sputter deposition but this point of view is clearly not shared in the ion beam community. Within this community, special efforts are taken to generate NOIs because it allows ion beams of mixed positive and negative ions to be produced and to avoid in this way surface charging during the bombardment [90, 91].

Despite the wealth of information produced under these driving forces, there is still no theoretical model that can predict the secondary ion probability with sufficient accuracy [75]. Hence, a full description will probably not be possible for each oxide and/or oxygen/plasma exposed surface. The reason for this lack is simple: the process is complex as the ionization of the sputtered particles is complicated by the dependence on the characteristic properties of the outgoing particles, the emitting surface, and the projectile ions as well as the mechanism of the ejection process. Various models have been proposed for a theoretical description of the ionization process. The models are typically described as a two-step process that involves first the ejection of atomic and/or molecular particles from the surface via knock-on sputtering. Evidence for this first step is given by investigations for negative ion emission with different bombarding ions, incident angles and ion energies. The agreement of the negative ion yield dependencies on these parameters with the Sigmund model [92] show that the O^- ions are emitted by the same mechanisms for the sputtering of neutral atoms [93]. As a second step of the negative ion emission mechanism, an electron transfer between the surface and the ejected particles is proposed. For example, it is generally accepted that a resonance charge transfer is the primary process responsible for atomic secondary ion formation/survival. The charge transfer occurs between a sputtered particle and the solid's surface as the sputtered particle departs the surface, i.e. during or shortly after the bond is broken between both players [94]. Two major models have been developed based on the resonant charge transfer: a bond-breaking approach for insulating substrates with (partially) ionic bonds between the constituent elements, while for (semi)conducting substrates with covalent or metallic bonds an electron tunneling approach is used.

A strong increase in the negative oxygen ion yield from metal surfaces exposed to oxygen is observed when the work function of the metal is reduced by the deposition of alkali metals such as Li or Cs on the target during the sputtering experiment [95, 96, 97]. In older work, the observation of negative oxygen ions and/or negative charged oxygen containing clusters was probably caused by the poorer vacuum conditions which led to adsorption of water and/or oxygen on the metal surface [98]. This contamination could be removed by heating the metal surface [99]. The enhancement by the deposition of

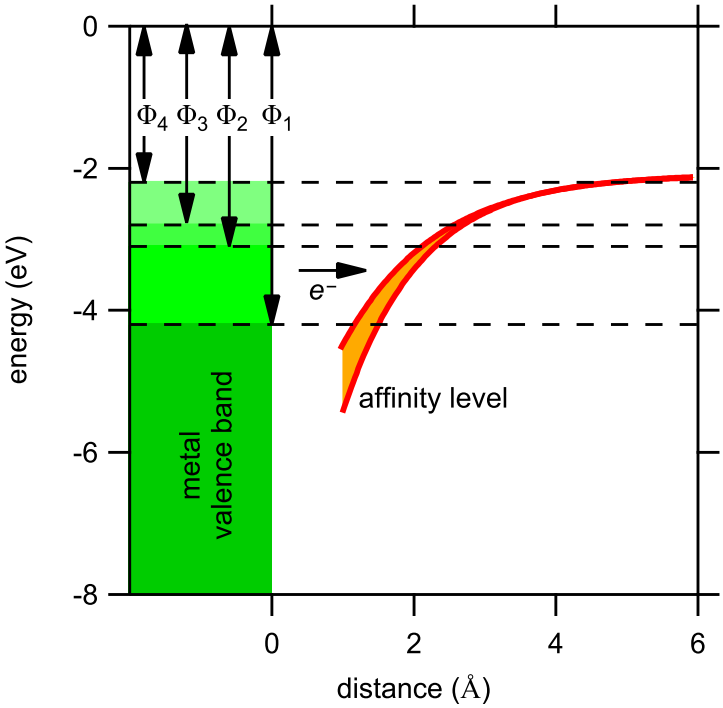

Figure 5. Schematic overview of the change of the affinity level (red lines) as a function of the distance versus a metal surface. The level width is indicated in orange. A simple band diagram of a metal (at 0 K) is presented in green. The deposition of alkali metal will result in a lowering of the work function Φ, or a raise of the Fermi level. A few positions of the Fermi level are shown.

alkali metals is typically described with the electron tunneling model. The electronic levels of an oxygen atom couple with the metal levels when the oxygen atom is close to the metal surface. The metal levels form a quasi-continuum of states and the atomic levels are degenerate with this quasi-continuum. As a consequence of the coupling, the atomic level acquires a finite lifetime or equivalently a width Δz. The interaction with the surface also results in shifts of the level energies which, as a first approximation, are understandable as image charge shifts. The coupling between atomic and metal levels induces an one-electron charge transfer process between the atom and the surface. It involves transitions with a constant energy and is usually termed 'resonant charge transfer' [100]. For the formation of negative ions, the level of interest is the electron affinity level of the atom leaving the surface (Figure 5). To tunnel from the metal to the affinity level of the atom, this level must correspond in energy with the occupied states in the metal. As the atom travels further from the surface, the affinity level increases to cross the Fermi level at some distance known as the crossing distance. To leave the vicinity of the metal surface as an ion, the ion must survive neutralization which is only possible when the width of the electronic level is sufficiently small [101]. In the case of O emission from a Cu or Al surface, the affinity level width (life time) is quite large (small) and hence the ionisation probability is small. By the addition of alkali elements, the work function is gradually reduced (see $\Phi_0 \rightarrow \Phi_1 \cdots$ in Figure 5) and the crossing distance increases. In this way not only the electron tunneling to the leaving oxygen atom can occur over a wide range of distances from the surface but also the probability it survives neutralization increases due to the longer lifetime. From Figure 5 it is clear that at some alkali metal coverage the survival probability will become unity [102]. Based on the above description, the work function dependence of the negative ion

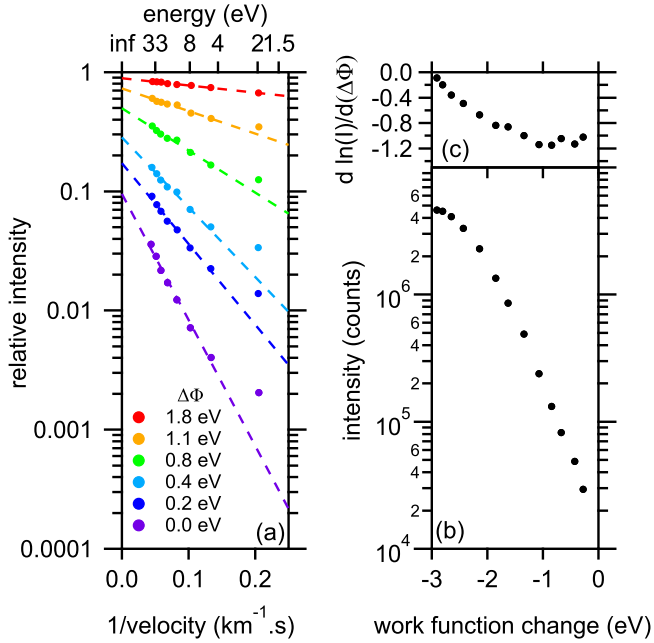

Figure 6. (a) The relative intensity of negative oxygen ions emitted from oxygen covered vanadium as a function of the inverse of the ion velocity (bottom axis)/energy (top axis). Experiments were performed at different Cs loading resulting in a shift of the work function. According to the tunneling model all lines should converge at the origin (data taken from Bernheim and Le Bourse [103]) (b) The intensity of negative oxygen ions emitted from oxygen covered vanadium (exposure 4 Langmuir) as a function of the work function change induced by cesiating the surface during 500 eV Ne^+ bombardment (data taken from Yu [95]). (c) The derivative of the data shown in (b), i.e. $d\ln(I)/d(\Delta\Phi)$ as function of the work function change.

yield can be written as [104]

$$\alpha^- \propto \exp\left(-\frac{\Phi - A'}{\epsilon_n}\right) \tag{12}$$

where A' and ϵ_n represent the electron affinity at the crossing distance from the surface and a parameter which depends on the particular ionization mechanism, respectively. This exponential dependence of the ionization probability on work function is however only a crude approximation within a limited range of $\Delta\Phi$. Indeed, based on Equation 12 it is expected that the derivative $d\ln(I)/d(\Delta\Phi)$ is constant. However, the derivative changes in some cases monotonically (Figure 6b,c) [102]. Moreover, a detailed analysis showed that the predicted inverse velocity dependence of the ionization probability fails at lower velocities where experiments reveal a velocity independent ionization probability [104]. The application of the tunneling model at high energy would lead to a probability independency of the work function which seems not to be confirmed by experiments (Figure 6a).

Deviations from the electron tunneling model can indicate the presence of additional excitation-based mechanisms. Many mechanisms have been described and discussed. Here, we focus on a specific example related to negative oxygen emission. The impact of low energy Na^+ (<500 eV) ions on Al covered with oxygen showed that both the electron and negative ion emission increases with increasing oxygen coverage [105, 106].

Na^+ ions were chosen to exclude potential electron emission from the metal surface [107, 108]. The low energy of the ions also reduces the probability of kinetic electron

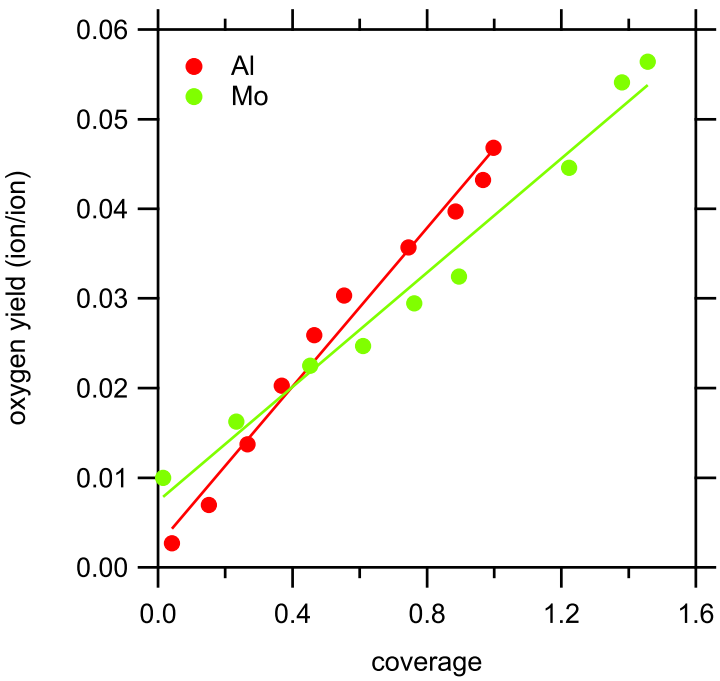

Figure 7. Negative oxygen yield for Na^+ on polycrystalline Al and Mo(100) surfaces as function of the surface coverage. The ion energy was 350 eV and 250 eV for the Al and Mo experiment, respectively. The negative oxygen yield data was taken from Tucek et al. [105](Al) and from Tucek et al. [109] (Mo). In these papers the negative ion yield is presented as function of the oxygen exposure. The latter was converted to an oxygen surface coverage using the oxygen adsorption studies for Al by Zhukov et al. [110] and for Mo by Riwan et al. [111]. The lines are linear fits through the data.

emission. Indeed, the observed energy distributions for both the electrons and negative oxygen ions can only be partially explained from direct kinetic emission (electrons) and a collision cascade (oxygen ions). The authors propose a collision induced excitation mechanism of the negative oxygen anion residing on the Al surface which leads to both electron emission and oxygen ejection. This mechanism is also used to explain the electron and ion emission for oxygen covered molybdenum surfaces [109]. The similarity between a single cyrstalline Mo(100) surface and a polycrystalline sample is used as a proof that for a significant secondary electron and negative ion emission, there must be oxygen on the metal's surface, but, to first order, it does not matter how the oxygen is bound. The study is further expanded to stainless steel (SS) surfaces. The latter can be important as most vacuum system are built from this material. Hence it is possible that low energy negative oxygen ions are released from the vacuum chamber walls which could affect the modeling of oxygen containing gas discharges [112, 113]. The same group has expanded the research to other metal/oxygen adsorbate systems such as W/O_2 [114] and Si/O_2 [115] bombarded with Na^+ ions. For Al, Mo, SS, and W the negative ion yield was determined for a fully covered surface. The yields at 250 eV Na^+ were equal to 0.044, 0.006, and 0.006, 0.022 for Al, Mo, SS and W, respectively. The NOI yield has also been measured as a function of the oxygen exposure. This means that this data can be used to investigate the correlation between the NOI yield and the oxygen surface coverage. Other studies have investigated the oxygen coverage as a function of the oxygen exposure for Al [110] and Mo [111]. The combination of these papers with the aforementioned results for the NOI yield is presented in Figure 7. It not only interesting to see that in both cases a linear correlation is found, but rather

similar slopes are observed.

When metal surface is bombarded by oxygen ion beams or by inert gas ions during oxygen exposure (known as flooding), the material surface becomes oxidized, i.e. in contrast to the previous sections, not only oxygen is chemisorbed on the top surface but also oxidation occurs within the subsurface. Simultaneously, a strong increase of both the positive metal ion and the NOI yield is observed [116, 117] (Figure 8). The pronounced yield enhancement is observed independently of whether the surface oxidation caused the work function to increase or decrease [104]. Another resonant charge transfer model for ionization, know as the bond breaking model, was suggested to explain the observed phenomena [118, 119]. The model is based on the idea that a description of an oxidized target surface in terms of continuous energy levels may not be appropriate. The sputtered particle may interact only with a few discrete electronic levels corresponding to the local ion bonds between the particle and the target atoms. In the model, ionization is assumed to result from breaking a partly ionic bond between the emitted atom and the oxygenated surface. This scenario has been discussed in terms of a crossing between the diabatic potential curves describing the interaction of an ionic and neutral particle with the surface. Diabatic means that there is no electronic interaction between the two covalent and ionic pairs. The model explains both the positive ion yield and the negative oxygen yield increase in agreement with the experiment (Figure 8). The sputtered oxygen atom leaves an anion vacancy at the surface. In case ionization occurs, the excess of positive hole must be trapped by this anion vacancy for a limited time to allow the oxygen atom to leave as a negative ion. An equation quite similar to Equation 12 can be derived [120]. The aforementioned reasoning can also be reversed to explain the emission of positive metal ions. According to Yu, the bond breaking model is similar in formulation as models based on the idea that the oxygen enhanced positive ion emission originates from the dissociation of sputtered, excited, neutral oxide molecules into a pair of positive and negative ions [119].

In some cases, not only the negative oxygen yield is increased but also the negative metal ion yield. To describe this behavior, adaptations to the bond breaking model are required. For example, in the surface polarization model [121], surface heterogeneity is introduced to tackle this problem. It postulates the existence of more complex types of bonding sites comprising at least next nearest neighbors which allows for rationalizing of both negative and positive ion yield enhancement with oxygen [122]. However, as the surface polarization model predicts a simultaneous decrease of the positive metal ion yield, in contrast to the experimental results (Figure 8) it has been challenged [123, 116]. The "anti-site" model has been suggested as an alternative which states that due to the bombardment some metal atoms will be present on anion sites, and hence can leave as a negative species [124].

As mentioned above, the explanation based on the image charge fails for insulating ionic surfaces and hence one would expect that the electron transfer from the surface to the atom is less favorable. Indeed, to allow an electron transfer from the ionic surface, the affinity level would need to shift more to align with the electron levels in the valence band. However, in contrast to a metal, the image attraction will be smaller. In strong resemblance with the bond breaking model, it can be argued that the downshift of the electron affinity level is in these cases still possible, even for strong ionic surfaces. In the latter case, the valence electrons are strongly bound to the oxygen sites, and therefore, the electron transfer from the surface to the leaving atom is mainly a local event where the electron moves to the atom from a particular oxygen site. As a result, this local site becomes a positive region on the surface which results in a Coulomb attraction that leads to the downshift required to bring the affinity level and the valence band

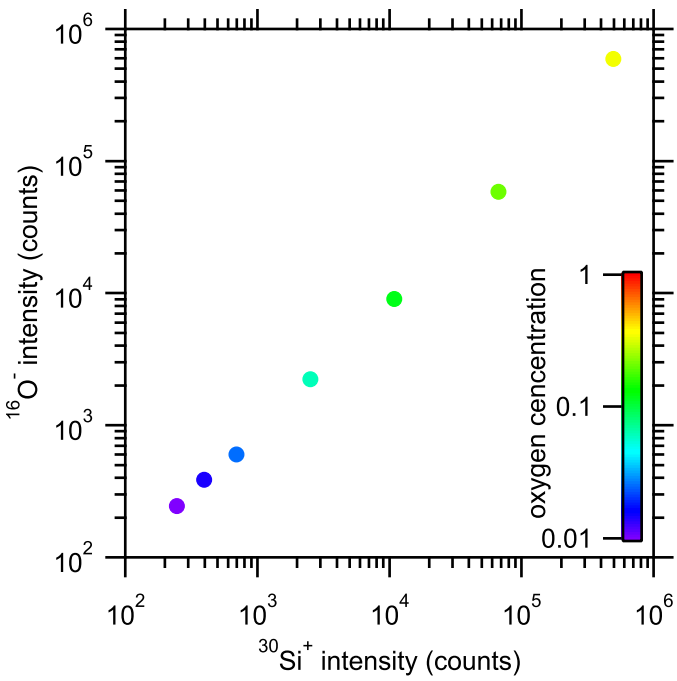

Figure 8. Correlation between the intensity for negative oxygen and positive Si ions emitted from silicon doped with different oxygen concentration (color scale) bombarded with 3 keV Ar ions. Data taken from Wittmaack [116].

into resonance [125]. As the negative ion moves away from the surface, it would still be possible that the reverse process, i.e., electron tunneling back into the material surface, occurs. However, the latter is less probable as the affinity level will overlap with the band gap between the valence and the condition band [126]. It should also be remarked that the aforementioned distinction between insulating and conducting surfaces should be handled with some care as in both models preferential sputtering of oxygen from the bombarded oxide surfaces will result in defect states located in the band gap of the solid [127] which could affect the description of the NOI mechanism.

5. Quantitative ion yields

The aforementioned mechanisms for negative ion formation at the target surface show a strong correlation between the work function and the negative ion yield. A similar correlation can be found for the ion induced electron yield [128, 129, 130]. This inspired researchers to investigate the correlation between negative ion and the electron yield [131]. It was shown for 13 different metals sputtered in DC reactive mode that the integrated intensity of the high energy peaks measured with a mass spectrometer (similar to the one shown in Figure 1) normalized to the sputtering yield of oxygen correlates with the ion induced electron yield measured for the poisoned targets. The correlation was confirmed for a few other metals [132]. This correlation indicates that the probability a sputter oxygen atom to leave the target surface as an ion is related to the electron yield of the same surface (Figure 9a). The used measuring method, i.e. mass spectrometry, hinders however to set up a quantitative correlation. As mentioned in section 2, the negative ion yield has been quantitatively determined during reactive magnetron sputter deposition for four materials: YBCO, ITO, CeO_2, and TiO_2. Also

the sputtering yields of these materials are known, and the electron yields can be calculated or have been published. A verification of the relation between the probability and the electron emission yield becomes in this way possible. Despite the limited number of data points in Figure 9a (blue points) a similar trend is observed which allows a quantification of the negative ion yield for a wide range of materials. A further test of this quantification can be made by a comparison between the calculated negative ion yields and another experimental data set. The absolute yield for the ejection of negative (and positive) ions from clean and oxidized surfaces of several metals was determined by Benninghoven et al. [141, 142, 143, 144]. An overview is shown in Figure 9b. The latter measurements have been made for 3 keV Ar^+ ion bombardment on metal surfaces exposed to oxygen. Under the assumption that the negative ion yield just scales with the impact energy, and a similar oxide layer is formed as during magnetron sputtering, it is possible to compare this data set with the calculated ion yields during reactive magnetron sputtering. A positive correlation between both data sets is found as shown in Figure 9c.

The negative oxygen yield for $BaTiO_3$ has been reported under the same conditions as used in the papers by Benninghoven et al. and has a value of 0.12. The correlation between the ion beam yields and the magnetron yields can be used to estimate the negative ion yield for magnetron sputter conditions. The electron yield was measured by Shintani et al. using a retarding field analyzer to understand the etching of a platinum substrate during DC diode sputtering from a $BaTiO_3$ target [145]. The authors attributed the observed etching to energetic neutrals but this result can now be explained by bombardment of negative ions [146]. The sputtering yield of $BaTiO_3$ is not reported at low energy. A rough estimate of the sputtering yield at a typical ion energy during magnetron sputtering (400 eV) can be made based on the reported ion etch rate at 2 to 3 keV assuming a linear dependence of the sputtering yield [147]. The result of the calculation is shown in Figure 9a with a green marker. Although this calculation is only made for one material and some rough estimates have been made, the reasonable agreement shows that the obtained data set seems to be consistent. Nevertheless, it should be mentioned that for some materials (Li, Mg, Y and YBCO) the ratio between the negative ion yield and the oxygen sputtering yield is larger than 1 (Figure 9a) which indicates that the error on the obtained results is probably large as a value larger than 1 indicates that more negative ions leave the material than can be sputtered. However, for two of these materials (Mg, Y) oxygen oversaturation during reactive sputtering have been reported which could indicate an additional negative oxygen emission mechanism based on outdiffusion of oxygen from the target [148].

The correlation between the electron and the negative ion yield holds an interesting guideline for deposition during reactive magnetron sputtering. As the discharge voltage is defined by the electron yield [136, 149], the formation of an oxide layer during target poisoning induces a change in the discharge voltage. A drop in the discharge voltage on poisoning indicates that the formed oxide has a higher electron yield than the metal, and hence it can be expected that negative ion bombardment can be important during film growth.

6. Trajectory of negative ions

High energy NOIs are generated at the surface of poisoned metal targets, or oxide targets during RF magnetron sputtering. They are accelerated over the cathode sheath. Their trajectory will for a great extend be determined by the orientation of the target surface.

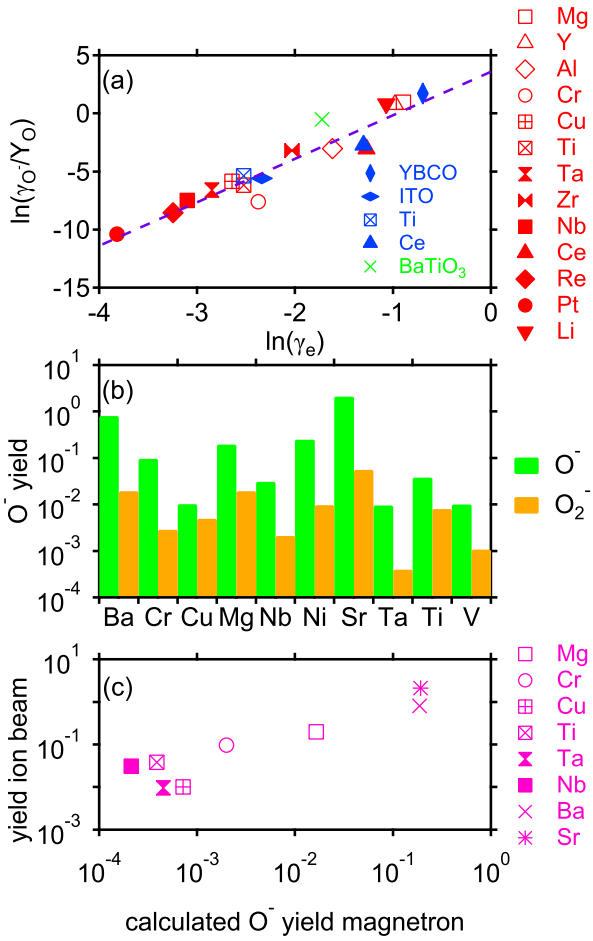

Figure 9. a) Correlation between the negative oxygen yield normalized to the oxygen sputtering yield, and the electron emission yield. The data represented in red markers has been taken from [131]. The blue markers are calculated based on the published data for the negative ion yield (YBCO [44], ITO [54], CeO_2 [58], TiO_2 [53]). The used sputtering yields were taken from experimental data (YBCO [133], ITO [134, 135], CeO_2 [136, 135], TiO_2 [136, 135]. For the electron yield experimental data was taken for YBCO [44] and CeO_2 [136], and TiO_2 [136]. For ITO, the electron yield was calculated based on published values for the work function [137].
b) The absolute yield for O^-(green) and O_2^- (orange) ions from oxidized metal surfaces. The yield was determined by static secondary ion mass spectrometry. The surface was oxidized at room temperature by exposure, expressed in Langmuir, to oxygen (Cr: 1600 L, Nb, Ta, V: 1000 L, Ba, Mg, Sr: 12000 L, and Cu, Ni, Ti: 1200 L). The exposure was sufficient to fully oxidize the polycrystalline surface. Ion bombardment was performed with a 3 keV Ar beam at an angle of 20° versus the surface.
c) The negative oxygen yield taken from figure b as a function of the calculated yield based on the correlation shown in figure a. Literature values for the electron yield for BaO [138] and SrO [139] were used. The sputtering yield for these materials were taken from Yoshimura et al.[140].

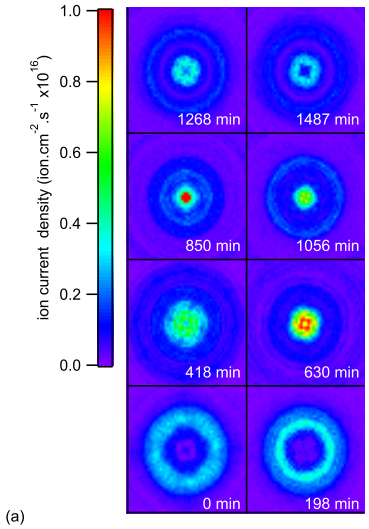

Figure 10. Simulated negative oxygen ion current density on a 5×5cm^2 substrate positioned 10 cm from a 2 inch circular planar target which is eroded for a different duration (as indicated per image). The target erosion profiles were taken from experimental work by our team[155]. Simulations were performed using SiMTRA [150, 151]. The starting positions of the 400 eV oxygen ions were weighted based on erosion groove. The ions were launched according the local normal direction. The argon pressure was equal to 0.5 Pa. The simulated discharge current was 0.5 A while the negative ion yield was set at 0.01.

This explains the differences observed in the usage of rotating cylindrical targets, the implementation of off-axis sputter deposition and facing target configurations, but also the impact of the target lifetime for planar magnetron configurations. The trajectory of the negative ions can be modeled with a simple ballistic approach where the ion follows a straight trajectory from its launching position on the target towards the growing film. To make the calculation more realistic, gas scattering could be included. During the discussion on target erosion, magnetron design, deposition configuration and conditions, test particle Monte Carlo simulations with the SiMTRA code will be used to guide the discussion [150, 151].

6.1. *Target erosion*

Several authors have reported on the change in film properties as function of the target lifetime. Examples are: film density and coloration of WO_3 films [152], texture evolution of ZnO [153], electrical properties of Al doped ZnO [19]. Measurements of the NOI count rate radially over a Zn target sputtered in poisoned mode shows that the negative ions are only emitted from the racetrack, and their trajectory depends strongly on the target lifetime [154]. The magnetic configuration of a magnetron results in a localized, toroidal shaped ionization region above the target. As the positive ions are not affected by the magnetic field, they travel in straight paths towards the target, and hence the target is locally eroded by sputtering. For planar targets, the erosion groove (or racetrack) becomes deeper during the target lifetime. In the case of a DC magnetron discharge, the full discharge voltage drops in the sheath which has in the case of a magnetron discharge a thickness of the order of 1 mm. As the sheath above the target follows the target surface profile, this means that the negative ions, accelerated over the sheath, will have a launch direction defined by the local orientation of the target surface. For a non-eroded, new target, the majority of the ions will be detected directly opposite to the racetrack. For a

strongly eroded target, the ions formed at the inclined surfaces of the erosion track will be launched in a non-normal direction, This will change the negative ion flux towards the growing film, and hence the film properties can depend on the target life time which is detrimental regarding the reproduciblity. Of course, not only the negative ion flux will change, but also other species such as sputtered atoms and reflected neutrals will be redirected. However, the nascent energy distribution of sputtered atoms and reflected neutrals has typical a cosine related distribution. Target erosion will modify the final distribution only to a minor extend [156]. Further, the contribution of reflected argon neutrals will be smaller for oxide and poisoned target surface due to lower, average atomic number. Reflected oxygen atoms are less important as the oxygen fraction in the gas discharge is typically below 20% during reactive magnetron sputtering.

The effect of the erosion profile on the distribution of the negative ions is modeled using the aforementioned particle trajectory code SiMTRA. To include the target erosion profile in the public version of this code the following strategy was followed. A 2 inch planar circular target was meshed in 24×180 trapezoidal cells. The orientation of each cell was calculated from experimental erosion profiles which were measured during the target life time [155]. The negative ions were launched in the normal direction for each cell with an energy of 400 eV. A square substrate (5×5 cm^2) was placed at a distance of 10 cm from the target. Both target and substrate were place in a cubic vacuum chamber (the simulation volume) with an edge length of 0.5 m. The argon pressure was set at 0.5 Pa. Figure 10 shows the result. The racetrack of a fresh target (0 minutes) is reflected on the substrate. As the target is more eroded, the ions gets more focused towards the center of the substrate to reach high current density (approx. 1.5 mA/cm^2 for an assumed discharge current of 0.5 A and a negative ion yield of 0.01) for a 850 minutes eroded target. Further erosion leads to a more even spreading of the ions of the substrate. The high ion current densities could lead to space charge effects as observed for low energy ion beams [58]. The result will depend on the details of the magnetic field configuration and the target-to-substrate distance.

The change of the launch direction due to the target erosion has also an important impact on the measurement of the negative ions using mass spectrometry as the latter has a low acceptance angle (Equation 6). Therefore, the interpretation of radial distribution of negative ions emitted from the target using mass spectrometry must be treated with some care. This has been demonstrated for the deposition of AZO thin films. While the radial distribution of the high-energetic negative ions as measured with the mass spectrometer showed two maxima opposite to the race track, the resistivities of the films only showed one maximum opposite the center of the target. While the mass spectrometer has a low acceptance angle of a few degrees, the sample has an acceptance angle of 90° which is the cause of this discrepancy [157]. The latter can also be proven using SiMTRA. The simulations show that for the deepest eroded target approximately 70% of the NOIs reach the 5×5 cm^2 substrate, i.e. a drop of 30% as compared to a fresh target. This effect is much stronger when the acceptance angle is limited to 1°. While 22% of the NOIs can be measured at the substrate position for a fresh target, only 2.5% will be measured for the deepest eroded target.

6.2. *Rotating cylindrical target*

The high energetic NOIs follow approximately a straight path from target to substrate. The formation of the erosion groove on a planar targets results in a concave surface which can lead to a different ion density profile on the sample as discussed in the

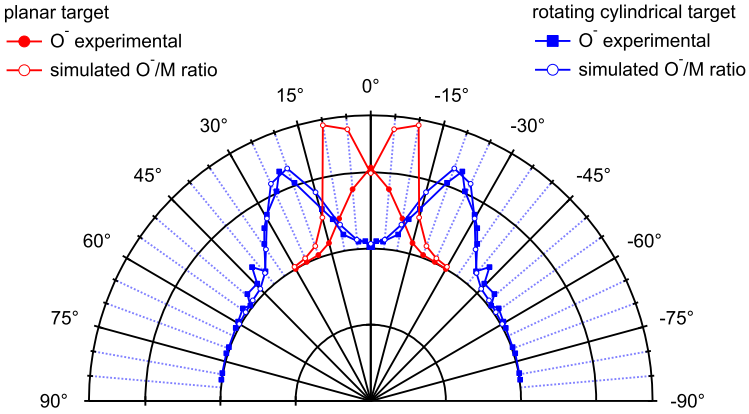

Figure 11. The angular distribution of negative oxygen ions as measured with a mass spectrometer during sputtering of Al in poisoned mode with a planar target (red closed markers) and a rotating cylindrical target (blue closed markers). The open markers show the simulated ratio between the negative oxygen and metal flux using SiMTRA. Data were taken from Mahieu et al. [33].

previous section. The surface of rotating cylindrical magnetron is however convex, and hence the angular distribution of the emitted negative ions will be different. The latter is confirmed by experiments [33] as shown in Figure 11. The angular distribution of ions emitted from a planar target peaks at 0°, i.e. at the center of the substrate position. The angular distribution of ions emitted from a rotating cylindrical magnetron shows two peaks, one for each leg of the racetrack. This difference in angular distribution was also demonstrated by a comparison of the properties of YBCO thin films located at different positions under a rotating cylindrical magnetron [158]. The trajectory of negative oxygen ions generated at a rotating cylindrical target has been calculated by an 2D PIC-MC simulation. The negative ions are ejected as sharp rays from the two legs of the racetrack in agreement with the above analysis, The simulations are linked to the increased resistivity of experimentally deposited Zn_2SnO_x thin films [159]. Similar simulations have been performed for a dual planar magnetron configuration showing the same beamlike behavior of the ejected negative oxygen ions [160].

6.3. *Strategies to reduce the impact of negative ion bombardment*

6.3.1. High pressure experiments

The idea behind an increasing of deposition pressure is to achieve more scattering of the negative oxygen ions, and hence less negative ions bombard the substrate. Krumme et al. [38, 39] have studied by mass spectrometry the pressure dependency of the negative oxygen ion flux for both YBCO and a bismuth-gadolinium-iron garnet targets. During DC sputtering at constant discharge power, the m/q=16 signal decreases for the high energetic NOIs, while remaining more or less constant for the low energy NOIs. The pressure dependency for RF is more complicated. The intensity of the low energy ions show a steep decline with increasing pressure. The signal for the high energy ions initially increases with pressure, but drops at high argon pressures. A similar behavior was observed when argon was replaced by krypton or xenon. The difference in behavior between DC and RF excitation should however be treated with some care because especially at high pressures the distinction between the low and high energy contribution for

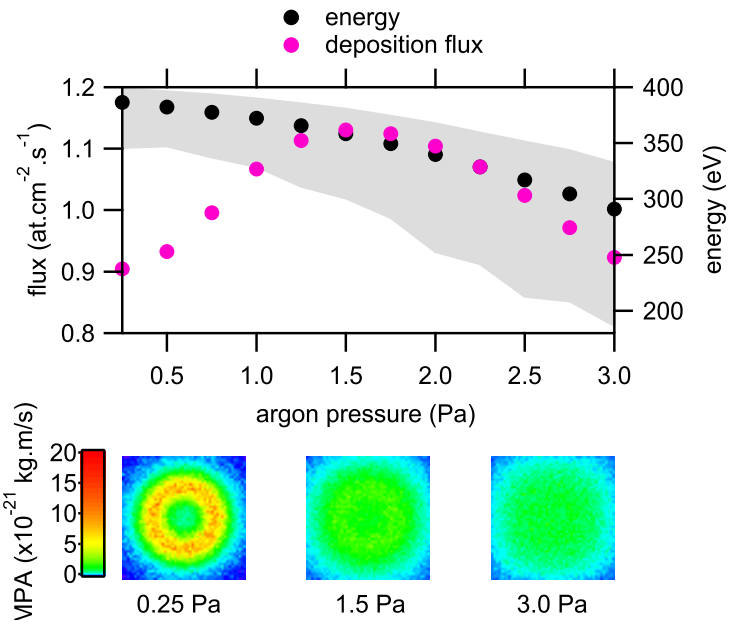

Figure 12. Simulation of the deposition flux (left hand axis, pink markers) and negative ion energy (right hand axis, black markers, grey background) as a function of the argon pressure. The grey region is defined by the lowest and highest ion energy arriving at the substrate. The bottom three figures give the distribution of the momentum per arriving atom (MPA) over a 5×5 cm^2 sized substrate located 10 cm the target. Simulation conditions were the same as for Figure 10 with a non-eroded target. Molybdenum (Mo) was chosen as transported element as its mass is close to the average of yttrium, barium and copper.

RF seems somewhat artificial as the peak energies become almost equal. As mentioned before, the interpretation of mass spectrometry results is complicated by the low acceptance angle of the device. Scattered negative ions are more difficult to detect, even if they have only lost part of their energy. Furthermore, at higher pressure, the probability of electron detachment (see section 3) increases, and the negative ions become energetic neutrals [47].

Most experimental work shows that very high pressures are required before negative ions get thermalized. The latter is also confirmed by the performed SiMTRA simulations. It is assumed in the simulation that the launching energy remains constant to disentangle the effect of pressure and the effect of ion energy. In real experiments however, the discharge voltage at higher pressure will be lower [161, 162], and as such also the launching energy. Other effects such as electron detachment in the cathode sheath could affect the ion energy because the maximum energy an ion obtains, is determined by how long it will retains its attached electron. However, this effect can be neglected as the cathode sheath is only of the order of a millimeter [163, 164, 165]. Moreover, the effect of the higher pressure (atom density) which enhances the probability for electron detachment, will be (partially) compensated by the narrowing of the cathode sheath as the deposition pressure increases [166]. Figure 12 shows the average energy of the NOIs that arrive on a 5×5 cm^2 substrate located at 10 cm from a 2 inch target. The average energy is close to the initial energy at low argon pressure, but at high pressure the energy of the ions is still very high as compared to displacement energies in materials. These simulations are in line with analytical calculations [163, 164]. For example at 3 Pa, the lowest simulated energy is still close to 200 eV. The deposition flux shows the typical behavior with a maximum as function of the argon pressure. The deposition rate decreases faster with increasing pressure than the average energy which means

that the gain in a reduction of the momentum flux towards the growing film ceases once the maximum in deposition rate has been reached. The latter can also be evaluated by the calculated the transferred momentum due to negative ion bombardment scaled per arriving metal as shown in the bottom images of Figure 12. The main effect of the increased argon pressure is a more evenly spreading of the momentum flux. Hence, it is more difficult to observe the behavior of the NOI impact as the substrate is more uniformly bombarded. Moreover, as mentioned before, a decrease of the discharge voltage during constant current/power experiments will be observed. Hence, the negative oxygen ion energy will decrease. Alternative strategies to lower the discharge voltage have also be suggested in literature. The change of the ion energy by changing DC powering to RF powering will be discussed further in the text. Another approach is to increase the magnetic field strength at the target [18, 167, 168].

6.3.2. Off-axis and facing target sputtering

Not only working at high pressure have been reported as a method to avoid negative oxygen bombardment during the deposition of YBCO thin films [169], but also off-axis sputtering [170], facing target sputtering [171], hollow cathode gas flow sputtering [172], and the usage of a mask between target and substrate have been applied [173, 174, 175]. In the case of off-axis sputtering, hollow cathode gas flow sputtering, and facing target sputtering, the substrate normal is perpendicular to the target normal, and in this way negative ions are hindered to reach the growing film. Target erosion can however in the case of off-axis sputtering result in an increase of the negative ion flux because ions launched from the inclined surface of the eroded target (subsection 6.1) can reach the substrate [170]. Some of these approaches have also been implemented for the deposition of transparent conducting oxides (TCOs): e.g. facing target sputtering for ITO [176, 177, 178, 179]. The impact of off-axis deposition on the opto-electronic properties of AZO films have been studied. The effects have been attributed to negative ion bombardment, but the influence of other deposition parameters such as the deposition rate and a possible effect of the chemical composition due to a difference in deposition profile of Al and Zn have not been evaluated [180]. Similar work was performed for Ga:ZnO [181]. The use of facing target dual rotating cylindrical magnetrons to deposit AZO have been reported to reduce the damage to $Cd(In,Ga)Se_2$ solar cells. To compensate for the low deposition rate, a bilayer was deposited with the magnetrons first in facing configuration, and then the magnet assembly was rotated to point directly towards the substrate [182].

A similar strategy to avoid negative ion bombardment is the use of a shield as demonstrated during the deposition of AZO films by RF magnetron sputtering using a oxide target [183].

6.3.3. Substrate bias

A negative bias on the sample to deflect the negative ions have been reported [184]. A more complex strategy to reduce the energy of the negative oxygen ions by an electric field is *magnetic field shielded sputtering*. The set-up includes a permanent magnetic array between the magnetron and the substrate holder. The plasma is confined between the magnetron and the array because electrons are trapped in the magnetic field of the array. As the array is electrically isolated, its potential becomes negative with respect to the plasma, and hence it limits the negative ions to impinge at full energy on the substrate [185].

7. Impact on thin films

The bombardment of the growing film with NOIs leads to several changes which are known and typical for sputter bombardment: i) material removal, or resputtering ii) preferential sputtering and hence compositional changes, iii) morphological, microstructural and textural changes. These effects are not limited to the growing film but can also affect existing thin films and devices, and can be subdivided under sputter damage [186]. This paper will mainly focus on the correlation between growing film properties and the presence of NOI bombardment.

Some papers attribute the observed changes in film properties to negative ions using the similarities with other studies but without actual proof for the presence of negative ions. The difference in deposition geometry only can already affect the relative number of impinging ions as illustrated in section 6. The observed behavior can also be influenced by other energetic species present in the gas discharge. The material dependency will express itself in the material sensitivity on ion bombardment but also in the ion energy, and the number of ions per film forming species arriving at the same substrate. The latter can be expressed as an ion-to-atom (ITA) ratio,

$$ITA = \frac{\gamma_{\mathrm{O}^-} I^+ f_{\mathrm{O}^-}}{Y_{\mathrm{c}} I^+ f_{\mathrm{c}}} \tag{13}$$

where γ_{O^-} represents the negative oxygen yield, Y_{c} the compound sputtering yield, I^+ the ion current on the target, and f_i the fraction of ions ($i = O^-$) or atoms ($i = c$) that arrive on the substrate, i.e. the transfer functions.

A benefit of this literature overview is the quantification of the NOI yield as obtained in section 5. The correlation between the probability for a sputtered oxygen ion to leave the oxidized target as a NOI, and the electron yield (Figure 9) can be used to calculate the negative ion yield for different metal target sputtered in poisoned mode, or for oxide targets sputtered in pure argon. The probability that a negative ion will arrive on the substrate, i.e. the transfer function, can be simulated using SiMTRA (see e.g. Figure 10 or Figure 12). In a similar fashion, it is possible to calculate the deposition rate by a combination of the same simulation geometry and the sputtering yield for the metal from the poisoned target. Values for the latter have been published for a wide range of metals [148]. The used deposition symmetry in the SiMTRA simulations was a two inch planar magnetron located 10 cm from a 5×5cm^2 substrate. The transfer function for the studied metals was on average 7% while for the energetic ions (400 eV) the transfer function was 80%. Figure 13a summarizes the calculations.

Multiplication of the ITA with the ion energy opens the possibility to study the influence of the ion impact by comparison with typical displacement energies. Figure 13b shows this scaled energy for a low (200 eV) and a high (1000 eV) energy. The two green lines refer to typical displacement energies for oxides [187, 188]. The comparison between the energy per deposited atom and the displacement energy was also used to set-up a structure zone diagram which included ion assisted deposition [189].

The two figures will be used to guide the discussion of the following subsections. The values should not be treated as absolute guidelines because for example all simulations were performed with identical conditions but the specific experimental set-up can have a strong impact on both ion energy, and the ion trajectory. Nevertheless, the discussed approach is applicable for future work and as relative statements can be made, some initial conclusions can be discussed already at this point. The high atom-to-ratio explains the historical role of the material research on YBCO in the quantification and

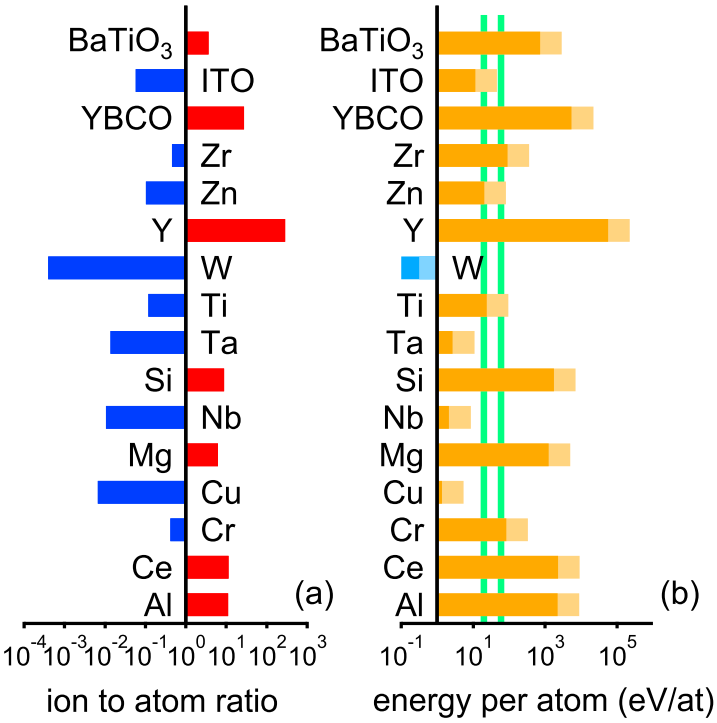

Figure 13. (a) The ion-to-atom ratio calculated for several materials. The negative ion yield was obtained from the correlation obtained in Figure 9. For WO_3 the calculated target condition [136] was used to calculate the work function of the reduced target state [191], and the electron yield. The sputtering yield was taken from literature [192]. For SiO_2 the sputtering yield was taken from Seah and Nunney [25]. The electron yield was calculated based on empirical equations [193]. A work function of 4.5 eV was used for ZnO to calculate the electron yield, realizing that the work function can strongly depend on the synthesis method, surface treatment, and surface cleanness. Literature values were used for the sputtering yield [194]. The transfer function of the negative ions was calculated using SiMTRA simulations using the same configuration as for Figure 12 at a pressure of 0.5 Pa. The same configuration was used to calculate the transfer functions for the different elements assuming a Thompson energy distribution and a cosine angular distribution. Except for ITO, $BaTiO_3$, and YBCO, the deposition rate was based on experimental sputtering yields for metal targets in poisoned mode. For ITO, $BaTiO_3$, and YBCO, the target was assumed to be sputtered without oxygen addition.
(b) The ion-to-atom ratio was multiplied with an ion energy of 200 eV (dark bars) and of 1000 eV (light bars). The two green lines indicate a low (20 eV) and high (60 eV) threshold for typical displacement energies for oxides [187, 188].

determination of NOI bombardment. The developed strategies during this research has been beneficial to improve the properties of TCO materials [146]. The impact of NOIs during the deposition of these materials became more challenging with the replacement of ITO by AZO. The latter material has a higher negative ion yield [190], and hence a higher ion-to-atom ratio can be expected (see values the larger values for aluminum and Zn as compared to ITO).

7.1. *Film texture*

Ion bombardment can lead to textural changes and the latter is also valid for NOI bombardment. For example, NOIs seem to control the the film texture of MgO thin films deposited by RF magnetron sputtering [195, 196]. Textural changes as function of the reactive gas flow are also often observed during reactive sputtering when the target state changes from metallic to poisoned. The strong drop of the deposition rate when

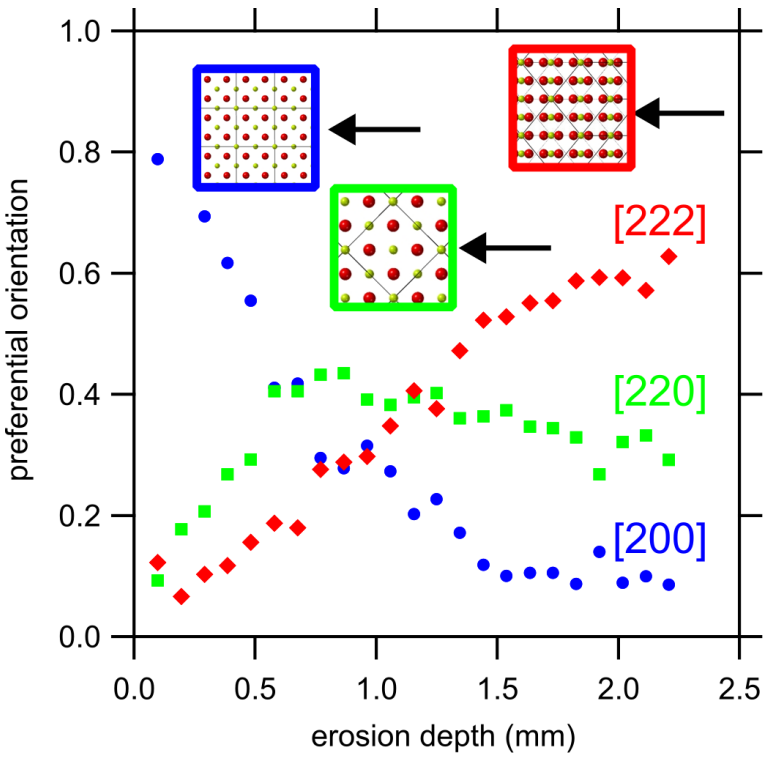

Figure 14. Texture coefficient for CeO_2 thin films deposited by reactive magnetron sputtering. The target was first sputter cleaned in pure Ar (pressure 0.5 Pa, discharge current 0.25 A, and pumping speed 108 L/s). 3 sccm of O_2 was added to fully poison the target. The insets show projections of the CeO_2 crystal structure. The arrow indicates the direction of the ions on the three surfaces. Data taken from Van Steenberge et al. [57].

the target poisons, strongly increases the flux ratio between the energy and material, or stated differently there is more energy available per deposited atom [197]. This typical transition was not observed during the growth of CeO_2. Films have a preferred [002] fiber texture independently when grown in metallic mode (low flux ratio) or poisoned mode (high flux ratio) [56]. This texture is expected in metallic mode as the growth is defined by an evolutionary overgrowth mechanism [197]. In poisoned mode, the growth is defined by surface energy concepts, and hence a [111] fiber texture is expected because the (111) surface has the lowest surface energy [198, 199]. The expected film texture in poisoned mode was only observed for deeply eroded targets. The transition from [002] to [111] fiber textured film as function of the target erosion depth (Figure 14) was accompanied with a decrease of the energy flux towards the growing film [57]. The latter is again unexpected as both for metal and reactive deposition typically an increase in the energy flux is observed when the target gets more eroded. Also the observed energy flux in poisoned mode is much higher than for Cu and TiN deposition at similar power and magnetron conditions [200]. Energy resolved mass spectrometry revealed a similar mechanism as in subsection 6.1, and allowed the additional energy to be attributed to the impact of NOIs. This means that for a fresh target the depositions are performed at high ion-to-atom ratio, and as discussed before, experiments are actually performed under ion-assisted conditions (Figure 13). The preferential growth under ion bombardment is explained from the higher projected atomic density in the [002] direction. When atomic density projected along a crystallographic direction is higher, the energy/momentum of the impinging ion is distributed over a larger number of atoms, and hence it is more stable against ion bombardment [201]. This mechanism has

the preference over a differential sputtering yield mechanisms as according simulations the latter evolves too slow to explain the texture evolution due to ion bombardment [202]. The origin in differential damaging relies, according these simulations, on the crystallographic nature of the channeling process. The latter is not a valid argument at low energy but the simulations probably set the correct time frame to distinguish between both mechanisms. The projected atomic density can be calculated based on the nuclear stopping radii which are energy dependent [201, 203]. The insets of Figure 14 show the result for three directions in the cerium oxide structure. The {220} surface is more packed, and hence more stable as compared to the other two orientations, but also the surface composition is important for the stability of the surface. In contrast to {220} the surface with the next most densest surface, {200} is oxygen terminated, and hence, the sputter removal of oxygen by ion bombardment can easily be compensated by oxygen adsorption from the oxygen/argon discharge. A similar reasoning was made for the preferential orientation of hydroxyapatite thin films. [204].

Eight different transition metal oxides were deposited in poisoned mode using DC magnetron sputtering [205]. Although no specific details were given regarding the film texture, it is reported that the oxides of V, Nb, Ta, W, and Mo grow amorphous while crystalline samples were obtained for Zr and Hf. Both crystalline and amorphous thin film were observed for Ti. As no other mechanisms could explain the trend, the authors attribute this behavior to energetic bombardment because they observe a similar trend in the film stress. The authors further state that the energy of the negative ions is much higher for the amorphous oxides because the discharge voltage increases on poisoning the target, while for the crystalline oxides the voltage increase is moderate. The observed trends are in-line with the model proposed in the beginning of this section. The high voltage in the poisoned mode indicates that the ion-induced electron yield for the target is low [136], and consequently also the probability to eject negative ions will be low. The trend is also clear from the ion-to-atom ratio or the calculated ion energy per atom (Figure 13). For W, Nb, and Ta a much lower value is calculated as compared to Zr. The value of Ti is in between the first group and Zr. This indicates that negative ion bombardment seems to assist the crystallization of titanium oxide. The above reasoning is further strengthened based on other results regarding the deposition of TiO_2 [206]. Off-axis sputter deposited thin films show a low crystallinity. Samples located above the racetrack of a new target are crystalline and are mainly composed of the rutile phase. As the arrival position of the NOIs change from above the racetrack towards the center of the racetrack due to target erosion, samples located above the racetrack of an old target are still crystalline but the anatase phase is more strongly observed, i.e. the reverse situations as for a new target. When the discharge power is changed from DCMS to HiPIMS, the phase composition shifts towards almost pure rutile. The study also investigates the role of ion bombardment with Xe^+ and O^+ ions to further proof the beneficial effect of ion bombardment on the crystallization of TiO_2 thin films. Strong ion bombardment should lead to amorphization which has been demonstrated for Y_2O_3 [33].

The aforementioned examples show that although some general trends can be explained, the specific role of NOI bombardment requires detailed analysis and the impact can be very material dependent. For example, several authors report on the impact of negative ions during the deposition of ZnO, although one would expect a relative low impact based on the calculated ion-to-atom ratio or calculated ion energy per atom (Figure 13). Nevertheless, several authors [207, 208, 209, 210, 211, 153, 212] report that the sample position relative to racetrack affects the ZnO film texture. Samples not facing the target racetrack often grow with the c-axis perpendicular, $c_\perp$, to the substrate

or the (0001) plane parallel with the substrate, while rather a $c_{\parallel}$ texture is observed for samples facing the racetrack. In the latter case, biaxial texturing with the $[11\bar{2}0]$ axis perpendicular to the substrate has been observed [213, 214]. A similar change in the texture has been observed when changing the magnetic balance from strongly balanced ($c_{\perp}$) to highly unbalanced ($c_{\parallel}$) which indicates that a strong energy flux towards the growing film favors $c_{\parallel}$ texturing [215]. As the NOI yield is expected to increase with target oxidation, the same conclusion can be made upon a comparison between low and high oxygen pressure experiments [216, 217], and the addition of aluminum during the deposition (see also further) [216]. The previously discussed strategies to avoid negative ion bombardment can be used to keep the $c_{\perp}$ film texture: working at higher total pressure [218], or by placing the samples parallel to the target normal [219].

A detailed study by Köhl [220] shows that in the case of ZnO, the film texture is mainly defined by the initial growth stage which can be influenced by ion bombardment [221]. Another argument for the nucleation driven selection of the film texture is the fact that annealing of $c_{\parallel}$ textured thin films doesn't result in a change of their texture but deposition at high temperature results in $c_{\perp}$ textured films [217]. The usage of heavy xenon ions with an energy of 800 eV results in the formation of $c_{\perp}$ textured films [222]. When this bombardment is only performed during the initial growth to form a seed layer, the film texture is not altered due to NOI bombardment [223]. This indicates that the (0002) layer is rather insensitive to negative ion bombardment. Auger electron spectroscopy and energy loss spectroscopy measurements show indeed that the ZnO(0001) surface is relatively resistant to the low energy argon ion bombardment-induced compositional changes [224]. No changes were observed for the Zn terminated surface, while a minor oxygen deficiency was observed for the O terminated surface. The latter can easily be compensated by the presence of oxygen in the magnetron discharge. The observation of the stable (0002) surface excludes mechanisms based on preferential sputtering, or on damage controlled selection as sometimes used in aforementioned references. Strong negative ion bombardment results in the formation of $c_{\parallel}$ textured seed layer which can be used in a similar fashion as for Xe bombardment to obtain for almost purely $c_{\parallel}$ textured films. The origin of the deteriorating effect of negative ion bombardment on the development of $c_{\perp}$ textured ZnO thin films is not fully clear but seems to be controlled by the energy, mass and current of the ions. This makes comparison between several studies difficult as for example a negative bias on the sample influences both the negative and the positive ion bombardment. Moreover, the presence of (carbon) impurities [225], the target state during long term deposition [210, 226] can further blur the general picture.

7.2. *Resputtering*

The impact of ions on a solid has been described/modeled and quantified in many ways. Hence, based on the aforementioned discussion on the ion energy, it can be expected that deposited material is again removed from the sample due to sputtering. In literature, this process is known as resputtering. In the earlier years of sputtering, the sputter removal by negative ions was already demonstrated by for example Jennings et al. who studied sputtering of Au deposited on oxidized tantalum anodes in a pure oxygen discharge [227]. Resputtering of ZnO was attributed to high energy neutral atoms [207], but later studies showed that origin of these neutrals are negative ions which are neutralized during their travel towards the growing film [48].

Also for AZO, resputtering was observed [228]. The impact of negative ion emission

on the thickness profile was studied during sputter deposition of $BaTiO_3$ [229]. Although no measurements were made regarding the presence of negative ions, the authors cite the similarity between this material and high temperature superconductors regarding NOI ejection. This similarity is indeed confirmed by the ion-to-atom calculations (Figure 13).

Figure 15a shows from the latter study the thickness profile for films deposited on a glass substrate as measured with profilometry. The grey line shows the expected deposition profile after 20 hours of sputter deposition. It is observed that the measured thickness is much lower in the region above the target. The change vs. the expected deposition profile is shown in Figure 15b. It is observed that the glass substrate gets etched at the beginning of the experiments. It must however be noted that the observed lowered deposition rate above the target/race track is not necessarily a direct proof for negative ion bombardment. For example, intensive electron bombardment can also induce the same effect [230]. In the latter study, a transverse magnetic field is used to avoid electron bombardment and hence to obtain a more uniform deposition. As the magnetic field is too weak to affect high energy negative ions, this result shows that NOI bombardment is in this specific case not the explanation for the reduced deposition rate. Substrate heating can also be an alternative explanation. An increased negative biasing of the substrate have been suggested by Hanak and Pellicane [231] as another alternative explanation. However, in the paper of Hanak and Pellicane, the results between on the one hand Y_2O_3 and Al_2O_3 targets are compared with on the other hand In_2O_3. The first two materials are known to have a high electron yield, and hence a high negative ion yield can be expected (Figure 9a) while for In_2O_3 the electron yield is expected to be much lower which is typical for semiconducting materials [136].

7.3. *Compositional changes*

Grace et al. discusses the role of NOI bombardment on the chemical composition of BSCCO thin films and the preferential loss of Bi [232, 233]. In both papers, no real evidence for negative ion bombardment is given, but the authors refer to similarity for YBCO targets with a preferential loss of Ba. Hirata et al. [234] illustrates a barium deficiency in barium for $YBa_{1.82}Cu_{2.85}O_x$ targets and a decrease of the deposition rate above the racetrack for $BaCu_{0.2}O_x$. For Y_2O_3 and CuO_x targets, the deposition rate decrease is not (or only slightly) observed. The '123' target composition has been enriched to '135' to compensate the barium (and copper) loss due to resputtering [235]. Experiments shows that hydroxyapatite coatings are deficient in P. Simulations show that the origin of this deficiency could be the resputtering effect due to NOIs [236]. Also, preferential sputtering of Zn from $Ta_2Zn_3O_8$ [237] and from AZO [238, 228], and of Ca from $Ca_3Co_4O_9$ [239] have been attributed to NOI bombardment.

7.4. *Morphological and microstructural changes*

Figure 16 shows a compilation of SEM micrographs of sputter deposited $BaTiO_3$ thin films [240]. The measurements were performed in a region where strong re-sputtering was observed (Figure 15). Micrograph a was taken closest to the center, while micrograph h corresponds to a spot on the substrate closer to the target edge. Black regions in micrograph a and b is the non-covered glass substrate. For position h a continuous, smooth film is observed. Etch pits, typical for ion bombardment, are noticed on the other micrographs which become stronger in density when the sample is closer to the target center. As a result, the surface roughness increases, and becomes defined by the

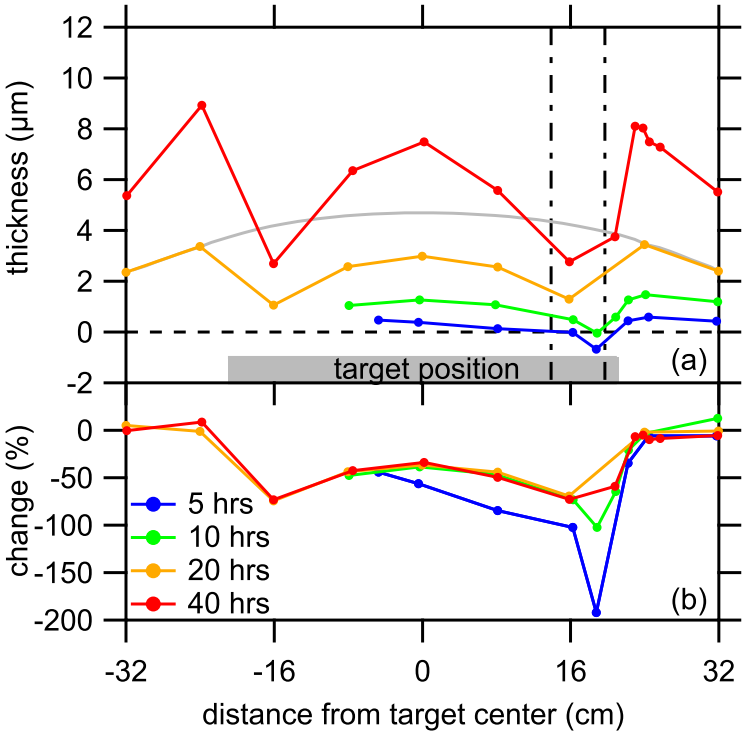

Figure 15. Figure (a) shows the measured thickness profile for $BaTiO_3$ film deposited by RF diode sputtering. The grey line is the expected deposition profile for 20 hours deposition when no resputtering would occur. Based on this latter reported profile, the expected profiles for the other deposited profiles were calculated, and used to calculate the relative change (Figure (b)). The vertical lines indicate the region the film were analyzed by scanning electron microscopy (see Figure 16). The deposition conditions are given in the caption of Figure 16. Data taken from Kester and Messier [229].

ion bombardment. The authors have studied the formation of the etch pits as function of the film thickness. For thicker films, surface ripples can be observed. Substrate etching have also been reported during sputter deposition of $SrTiO_3$ [241].

Densification of amorphous SiO_2 thin film by negative oxygen ion bombardment has been demonstrated [242].

7.5. *Functional film properties*

As demonstrated in section 6, the flux of NOIs depends strongly on the relative position of the substrate versus the target. Hence, it can be expected to observe a spatial variation of the functional properties which has indeed been demonstrated by several teams [18, 243]. Especially popular are AZO thin films deposited by magnetron sputtering using a metallic target [244] or a ceramic target [245, 246, 247]. The observed changes in crystalline quality, resistivity [248, 238, 249, 250] and, carrier concentration can be explained from the high energetic NOI bombardment. A stronger effect is observed for $Mg_{1-x}Zn_xO$:Al (with 10 %mol of MgO) as compared to ZnO:Al (with 2 %mol of Al_2O_3) [251]. This strong impact of NOI for ZnO is not really expected as the calculated energy per atom (Figure 13) for zinc is only marginal above the displacement energy threshold. However, in most of the aforementioned studies, the ZnO target has been doped with a few weight percent of Al (or Mg). Both Al_2O_3 and MgO have a much lower sputtering yield as compared to ZnO. This imbalance between the sputtering yields will result

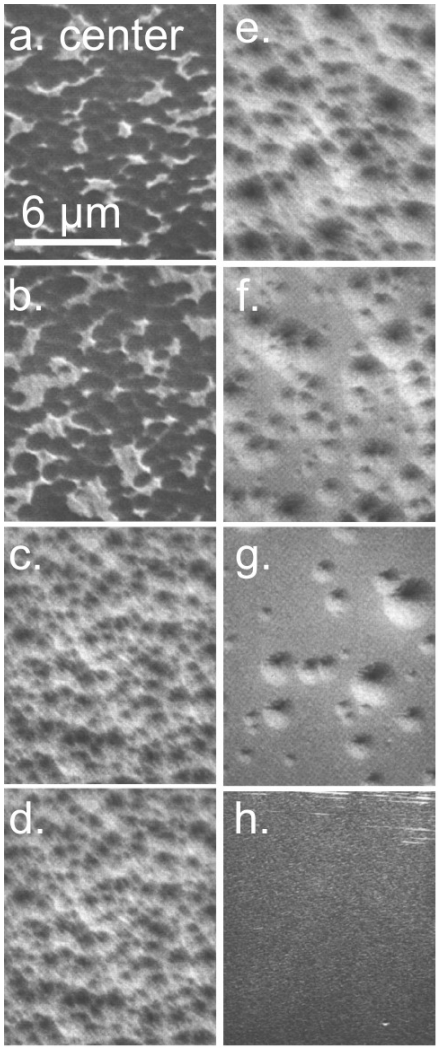

Figure 16. Micrographs of sputter deposited $BaTiO_3$ deposited by RF diode sputtering. Deposition conditions: 5 hours deposition, target-substrate distance 3 cm, power 100 W, total pressure 2.66 Pa, 1:1 argon:oxygen mixture. The micrographs were taken in a region indicated in Figure 15. The micrographs are ordered as function of the radial distance from the center of the target with micrograph a is taken closest to the target center. Compilation based on images provided by Kester and Messier [240].

in preferential sputtering of ZnO, and surface enrichment of the low sputtering yield material. The surface concentration ratio between ZnO and the dopant oxide can be calculated as [252, 24]

$$\left(\frac{C_{\text{dopant}}}{C_{\text{ZnO}}}\right)^{s} = \frac{Y_{\text{ZnO}}}{Y_{\text{dopant}}}\left(\frac{C_{\text{dopant}}}{C_{\text{ZnO}}}\right)^{b} \tag{14}$$

where Y_i is the sputtering yield, C_i the concentration, and the superscript s and b refer to the surface and bulk, respectively. Based on the reported values of the sputtering yield of Zn, Al and Mg sputtered in poisoned mode [148], the ratio of the sputtering yield can be calculated as 50 and 19.5 for aluminum oxide vs. ZnO and MgO vs. ZnO, respectively. Due to these large values, the surface is mainly covered with Al_2O_3 or MgO which both have a high NOI yield. This can probably also explain the difference in behavior between doped and undoped ZnO [216]. However, the difference in XRD domain size for AZO and ZnO thin films deposited under identical conditions has been attributed to the local environment of Al atoms which triggers a structural reorganization in the AZO thin films [253] but in this study the strong difference in NOI bombardment was not taken in consideration.

Differences in the NOI energy should also be considered to explain the functional properties. This was demonstrated for a-InGaZnO thin film transitors [43, 254, 255] and for AZO thin films [256]. The detrimental impact of NOIs can also mitigated by controlling the ion energy. It is for example argued that by lowering the discharge voltage, and hence the NOI energy, during DC sputter deposition of ITO fewer interstitial defects are generated [18]. Due to the shallower implantation of the oxygen into the growing film, the defects can be annealed at a higher rate during film growth. The NOI energy can also be modulated by choosing for an another excitation method of the magnetron discharge. This method was not discussed in subsection 6.3 but will be highlighted here due to the clear correlation between the NOI energy and the functional properties of TCO's. The average NOI energy dropped from 443 eV DC to 156 eV (RF 13.56 MHz) and 57 eV for RF 27 MHz during the deposition of AZO. [257, 258]. To lower the discharge voltage to even lower values, a high frequency RF (81 MHz) was superimposed to the DC power [259]. Experiments in the latter study were performed at constant DC power. The higher total discharge power resulted in a higher substrate temperatures at higher fraction of RF power. Nevertheless, the wide range in discharge voltages allowed the authors of this study to demonstrate an optimum discharge voltage. The films deposited at too low discharge voltage (<50 eV) remained underdense despite the higher substrate temperature at lower discharge voltages. Within the window of 60-110 eV the Hall mobility is maximal, and the drop of mobility above 110 eV is accompanied with a change from tensile to compressive film stress which confirms the detrimental impact of high energy NOIs. The effects indicate that the film properties are related to the momentum of the negative ions, and not to the overall energy flux towards the film. This conclusion is further substantiated by the observation that the lower boundary of the optimized window coincides with reported threshold displacement energies for ZnO which have an average energy of ≈50 eV (for Zn:43 eV, for O: 58 eV) [262, 263, 188, 187, 264, 265].

As discussed in subsection 6.1, the NOI flux depends on the position of the substrate above a planar target and results in this way in a spatial variation of the film properties. Hence, it becomes possible to investigate the material properties as function of both the ion energy, defined by the discharge voltage, and the ion flux, defined by the position above the target. Figure 17 shows the result of such a study for a few selected properties

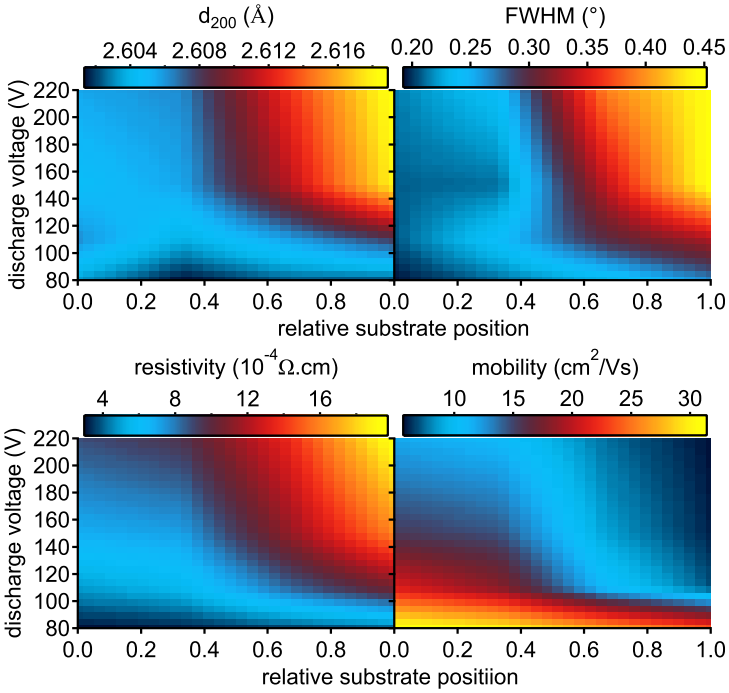

Figure 17. The d_{002} lattice spacing for AZO, the full width at half maximum (FWHM) of the (002) peak in the diffraction pattern, film resistivity and Hall mobility as function the relative substrate position and the discharge voltage. The discharge voltage was controlled by combining DC and RF (81 MHz) powering of a magnetron with a ceramic AZO target. The substrate position is defined relative to the target center (0) and the target erosion groove (1). The lattice expansion is attributed to the generation of various supersaturated point defects such as interstitials and vacancies [260]. An increase of the FWHM is related to a drop of the domain size which can be understood from the structural damage induced by ion bombardment. Figures based on the data presented by Meng et al. [261].

of AZO. Although the NOI flux was not quantified, the result clearly shows that at low flux, i.e. above the target center (relative position 0), the impact and the dependency of the ion energy is weak. Even more interesting is to observe that the ion flux dependency vanishes at low ion energy. While only special deposition strategies can be used to lower the ion flux (see subsection 6.3), a control by the ion energy seems a better strategy to optimize the film properties. The method was also applied to improve the properties of gallium doped zinc oxide, but the study showed that a direct transfer of the optimized deposition conditions for AZO is not possible [266].

The optical properties of Al_2O_3 were related to negative ion bombardment during reactive sputtering of an aluminum target in argon/oxygen mixture [33].

Plasma display panels (PDP) are currently replaced by LCDs as around 2013-2014 major companies such as Panasonic, LG and Samsung discontinued plasma TV production. The long term stability of PDPs has always been an issue. The phosphor degradation determined the luminace lifetime of a flat panel display. The degradation has been studied in detail by many teams and it has been shown that it is a complex process induced by many species such as UV photons, electron bombardment [267], and sputter deposited material from the cathode [268]. One of the reported species are also negative ions [269]. To lower the sustaining voltage of these panels, researchers have mainly searched for oxide materials with a high ion induced secondary electron emission yield such as MgO [270], but these materials have as such also a high negative ion

yield (Figure 9). This brings the investigation to an impasse: increasing the power efficiency by lowering the sustaining voltage will result in more negative ion bombardment. Although not proven, this impasse is perhaps one of the reasons the PDP technology has been abandoned.

7.6. *Thin film stress*

The impact of high energetic species can induce intrinsic film stress [271]. This has also been demonstrated for negative ion bombardment. As discussed in subsection 7.1, a correlation was observed between the ion-to-atom ratio and thin film stress for several transition oxides, reactive sputter deposited from metallic targets [205]. The stress of ITO thin films is attributed to negative oxygen ions and can be controlled by the deposition pressure [272]. A similar result was obtained for ZnO deposited by diode and magnetron sputtering [209].

8. Other negative ions

This paper gives a detailed overview of studies performed on the production mechanisms and the role of NOIs during reactive sputter deposition. Other electronegative elements can become a negative ion, and similar mechanisms as discussed for oxygen have been observed. Without the intention to go in the same detail, a short overview of studies focusing on other negative ions will be treated in this section.

The discussion will be guided based on the model discussed in the introduction [5, 6]. According to this model, the difference between the metal ionization energy (IE_M) and the electron affinity of the atom which leaves as negative ion (EA_X) defines the negative ion production. Based on the quantification of the negative ion yield for oxides (section 5) it becomes possible to test this model. Figure 18 shows the same data as Figure 9a but now plotted as function of the difference between metal ionization energy and electron affinity. For complex compounds such as $BaTiO_3$, YBCO and ITO the element with the lowest ionization energy was taken. A clear correlation is found with as major outliners MgO and Y_2O_3. The proposed threshold of 3.4 eV in the original model agrees with presented results (see striped orange line labeled threshold). This correlation, although in a more qualitative way, have been used by others to explain their observations. As mentioned before, the effects of resputtering of oxides was evaluated [7]. Also, the relative intensity of mass spectrometry results for five different oxides could be related to energy-affinity difference [12]

A remarkable illustration of negative ion bombardment is the co-sputtering of a planar circular target composed of ZnS with a smaller target of TbF_3 placed in the center of the larger target [231]. The substrate (unknown material) is according to the study etched by negative F^- while no etching is observed for outer part of the substrate. This observation corresponds with the prediction based on the difference between ionization energy and electron affinity (see labels TbF_3 and ZnS in Figure 18).

Re-sputtering of $(Ca_{0.55}Sr_{0.45})_{1-y}Ga_2S_4:Ce_y$ was observed and attributed to negative sulfur ion bombardment [273]. The same authors report also re-sputtering of SrS:Ce films and could control the re-sputtering rate by adjusting the discharge voltage. No re-sputtering was reported for ZnS. Again these observations are in line with the model presented in Figure 18. In the context to deposit absorber materials for thin solar cells, several sulfides and selenides which belong to the class of layered semiconductors have been investigated. Despite the potential of this approach, the research is limited to

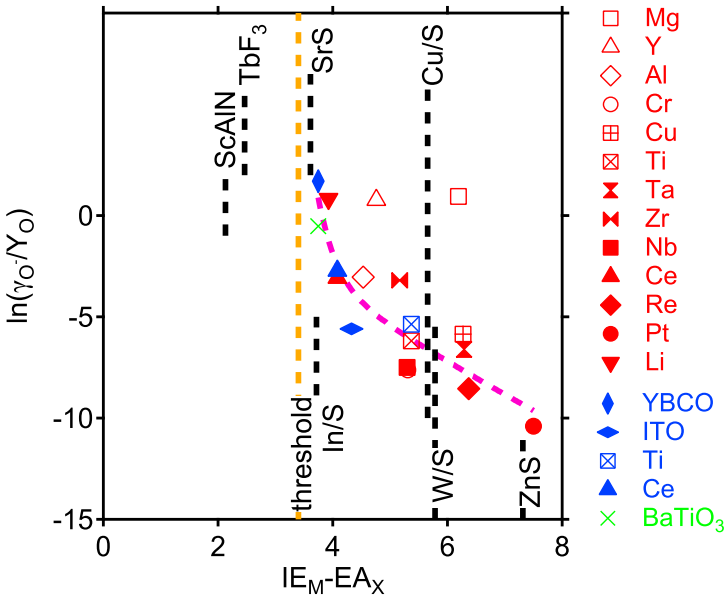

Figure 18. The data presented in Figure 9a plotted as function of the difference between the ionization energy of the metal M and the electron affinity of the atom X that leaves as a negative ion. The smallest difference is taken for complex materials. The striped line through the data points is not a fit but rather a guide for the eyes. Some of non-oxide compounds discussed in the text are also presented as a striped black line. Ionization energies and electron affinities were taken from literature [274].

the efforts of one team. Reactive sputtering with H_2S requires some additional technical efforts as the gas is toxic. The team has mainly investigated the growth of WS_2 [275, 276, 277, 278], MoS_2 [279] and $CuInS_2$ [280]. Measurements of the ion energy distributions with mass spectrometry were performed [281]. The studies on WS_2 discuss a possible effect of the negative ion bombardment, although it cannot be neglected that reflected neutrals also affect the film growth. The ion distributions of S^- are similar for both reactively sputtered W and Cu. The latter can be understood from their similar value in ionization energy. No information was given for In, although based on Figure 18 one would expect a stronger negative ion emission. Nevertheless, the authors indicate that the ion induced damage during the deposition of $CuInS_2$ is less pronounced, but a proper evaluation is difficult as some experimental details such as discharge voltage and current are missing.

The presence of CN^- during the deposition of ScAlN has been reported [282]. The origin of these ions have been attributed to presence of impurities such as C and O in the Sc ingots which were used as insert in the Al target. No chemical analysis of the ingots has been represented but it is interesting to observe that the negative oxygen intensity is much lower as compared to the CN^- intensity which qualitatively agrees with the difference in ionization energy and electron affinity. The authors also observe, although at much lower intensity, the same negative ions during the deposition of pure AlN, i.e. without Sc ingots, but no explanation is given regarding their origin.

9. Conclusions

Thin film growth by energetic deposition techniques, such as reactive (magnetron) sputter deposition, has been developed to expand the possibilities of non-energetic techniques. Bombardment with energetic species such as reflected neutrals, sputtered atoms, plasma ions can assist in the improvement of some specific film properties. The researcher has a tool to control the flux/energy of these species by mainly adjusting the target-to-substrate distance, the deposition pressure, and substrate bias. Negative ions that are accelerated over the cathode sheath have high energy and therefore alternative approaches are required to control their impact. A different deposition geometry and/or alternative discharge excitation methods have been used to control, or better to avoid, their impact. Where modeling can assist in the quantification of the number, energy, and direction of sputtered and reflected neutrals arriving at the growing films, quantification of the impact negative ions is more cumbersome. Illustrative for this point is that among the massive amount of literature on their (possible) impact on film properties, only a handful of studies have aimed to quantify the negative oxygen ion yield under (magnetron) sputter conditions. Nevertheless, combining this scarce knowledge acquired in the research community was sufficient to develop a more quantitative approach in this review paper. Although the scatter on the data is large, it is surprisingly that most of the experimental studies follow the calculated trends, and than even predictions based on a small number of measurements seems to hold when applied on a larger data set. This shows that the future is bright as it can be expected that new quantification attempts will confirm the presented trends. The proof of the pudding is in the eating. This review should not be an endpoint, but a starting point in further exploring the role of negative ion bombardment, and in the quantification of (magnetron) sputter deposition.

Acknowledgement(s)

This work is dedicated to two researchers who have passed away recently, and had a major impact on the scientific career of the author. The first researcher is Professor Johan (Jo) Haemers, member of the same department, who assisted the research of the author in the development of special measuring set-ups, and in long discussions on science and other important things in life. The second researcher is Professor Joseph (Joe) Greene. His research approach, presentation style, and his interest in old and recent scientific literature was an example to many and to the author in particular.

Disclosure statement

The author declares that there are no relevant financial or non-financial competing interests to report.

Funding

This research received no specific grant from any funding agency in the public, commercial, or not-for-profit sector.

References

[1] J. E. Greene, Review article: tracing the recorded history of thin-film sputter deposition: From the 1800s to 2017, Journal of Vacuum Science &Technology A: Vacuum, Surfaces, and Films 35 (5) (2017) 05C204. doi:10.1116/1.4998940.

[2] W. R. Grove, VII. on the electro-chemical polarity of gases, Philosophical Transactions of the Royal Society of London 142 (1852) 87–101. doi:10.1098/rstl.1852.0008.

[3] F. L. Arnot, C. Beckett, A new process of negative ion formation. IV, Proceedings of the Royal Society of London. Series A. Mathematical and Physical 168 (932) (1938) 103–122.
URL https://www.jstor.org/stable/97171

[4] R. E. Honig, Sputtering of surfaces by positive ion beams of low energy, Journal of Applied Physics 29 (3) (1958) 549–555. doi:10.1063/1.1723219.

[5] J. J. Cuomo, R. J. Gambino, J. M. E. Harper, J. D. Kuptsis, Origin and effects of negative ions in the sputtering of intermetallic compounds, IBM Journal of Research and Development 21 (6) (1977) 580–583. doi:10.1147/rd.216.0580.

[6] J. J. Cuomo, R. J. Gambino, J. M. E. Harper, J. D. Kuptsis, J. C. Webber, Significance of negative ion formation in sputtering and SIMS analysis, Journal of Vacuum Science and Technology 15 (2) (1978) 281–287. doi:10.1116/1.569571.

[7] D. J. Kester, R. Messier, Predicting negative ion resputtering in thin films, Journal of Vacuum Science & Technology A: Vacuum, Surfaces, and Films 4 (3) (1986) 496–499. doi:10.1116/1.573867.

[8] D. O'Connell, R. Zorat, A. R. Ellingboe, M. M. Turner, Comparison of measurements and particle-in-cell simulations of ion energy distribution functions in a capacitively coupled radio-frequency discharge, Physics of Plasmas 14 (10) (2007) 103510. doi:10.1063/1.2795634.

[9] M. H. S. Low, C. H. A. Huan, A. T. S. Wee, K. L. Tan, An alternative method for determining the transmission function of secondary ion mass spectrometers, Nuclear Instruments and Methods in Physics Research Section B: Beam Interactions with Materials and Atoms 103 (4) (1995) 482–488. doi:10.1016/0168-583x(95)00665-6.

[10] N. Martin, A. R. Bally, R. Sanjinés, F. Lévy, Intrinsic low energy bombardment of titanium chromium oxide thin films prepared by reactive sputtering, Surface and Coatings Technology 130 (2-3) (2000) 280–289. doi:10.1016/s0257-8972(00)00672-1.

[11] N. Martin, A. M. E. Santo, R. Sanjinés, F. Lévy, Energy distribution of ions bombarding TiO_2 thin films during sputter deposition, Surface and Coatings Technology 138 (1) (2001) 77–83. doi:10.1016/s0257-8972(00)01127-0.

[12] K. Ishibashi, K. Hirata, N. Hosokawa, Mass spectrometric ion analysis in the sputtering of oxide targets, Journal of Vacuum Science & Technology A: Vacuum, Surfaces, and Films 10 (4) (1992) 1718–1722. doi:10.1116/1.577776.

[13] T. Welzel, K. Ellmer, Comparison of ion energies and fluxes at the substrate during magnetron sputtering of ZnO:Al for dc and rf discharges, Journal of Physics D: Applied Physics 46 (31) (2013) 315202. doi:10.1088/0022-3727/46/31/315202.

[14] N. Ito, S. Miyatake, N. Tsukamoto, N. Oka, S. Sato, Y. Shigesato, In-situ analyses on reactive sputtering processes to deposit photocatalytic TiO_2 films, Japanese Journal of Applied Physics 49 (4R) (2010) 041105. doi:10.1143/jjap.49.041105.

[15] M. Y. Hur, J. K. Kim, H. J. Lee, The effect of negative ions from the target on

thin film deposition in a direct current magnetron sputtering system, Thin Solid Films 587 (2015) 3–7. doi:10.1016/j.tsf.2015.03.019.

[16] T. Ishijima, K. Goto, N. Ohshima, K. Kinoshita, H. Toyoda, Spatial variation of negative oxygen ion energy distribution in RF magnetron plasma with oxide target, Japanese Journal of Applied Physics 48 (11) (2009) 116004. doi:10.1143/jjap.48.116004.

[17] B. Chapman, Glow Discharge Processes: Sputtering and Plasma Etching, Wiley, 1980.

[18] S. Ishibashi, Y. Higuchi, Y. Ota, K. Nakamura, Low resistivity indium-tin oxide transparent conductive films. II. Effect of sputtering voltage on electrical property of films, Journal of Vacuum Science & Technology A: Vacuum, Surfaces, and Films 8 (3) (1990) 1403–1406. doi:10.1116/1.576890.

[19] N. Tsukamoto, D. Watanabe, M. Saito, Y. Sato, N. Oka, Y. Shigesato, In situ analyses on negative ions in the sputtering process to deposit Al-doped ZnO films, Journal of Vacuum Science & Technology A: Vacuum, Surfaces, and Films 28 (4) (2010) 846–850. doi:10.1116/1.3430556.

[20] J. Jia, Y. Torigoshi, Y. Shigesato, In situ analyses on negative ions in the indium-gallium-zinc oxide sputtering process, Applied Physics Letters 103 (1) (2013) 013501. doi:10.1063/1.4812668.

[21] M. Zeuner, H. Neumann, J. Zalman, H. Biederman, Sputter process diagnostics by negative ions, Journal of Applied Physics 83 (10) (1998) 5083–5086. doi:10.1063/1.367325.

[22] M. W. Thompson, Atomic collision cascades in solids, Vacuum 66 (2) (2002) 99–114. doi:10.1016/s0042-207x(02)00179-3.

[23] M. P. Seah, M. W. Holbourn, C. Ortega, J. A. Davies, An intercomparison of tantalum pentoxide reference studies, Nuclear Instruments & Methods in Physics Research Section B-Beam Interactions with Materials and Atoms 30 (2) (1988) 128–139. doi:10.1016/0168-583x(88)90109-7.

[24] J. B. Malherbe, S. Hofmann, J. M. Sanz, Preferential sputtering of oxides - a comparison of model predictions with experimental-data, Applied Surface Science 27 (3) (1986) 355–365. doi:10.1016/0169-4332(86)90139-x.

[25] M. P. Seah, T. S. Nunney, Sputtering yields of compounds using argon ions, Journal of Physics D-Applied Physics 43 (25) (2010) 253001. doi:10.1088/0022-3727/43/25/253001.

[26] W. Möller, W. Eckstein, J. P. Biersack, Tridyn - binary collision simulation of atomic-collisions and dynamic composition changes in solids, Computer Physics Communications 51 (3) (1988) 355–368. doi:10.1016/0010-4655(88)90148-8.

[27] J. F. Ziegler, J. P. Biersack, M. D. Ziegler, SRIM - The Stopping and Range of Ions in Matter : www.srim.org, SRIM, 2012.

[28] A. Goehlich, M. Röwekamp, H. F. Döbele, Determination of the velocity distribution of sputtered atomic oxygen by laser-induced fluoresence in the vacuum-ultraviolet (130 nm), Surface Science 248 (1991) 271–275. doi:10.1016/0039-6028(91)90080-C.

[29] M. Stepanova, S. K. Dew, Anisotropic energies of sputtered atoms under oblique ion incidence, Nuclear Instruments and Methods in Physics Research Section B: Beam Interactions with Materials and Atoms 215 (3) (2004) 357 – 365. doi:10.1016/j.nimb.2003.09.013.

[30] M. Stepanova, S. K. Dew, Estimates of differential sputtering yields for deposition applications, Journal of Vacuum Science & Technology a-Vacuum Surfaces and Films 19 (6) (2001) 2805–2816. doi:10.1116/1.1405515.

[31] P. Pokorný, M. Mišina, J. Bulíř, J. Lančok, P. Fitl, J. Musil, M. Novotný, Investigation of the negative ions in Ar/O_2 plasma of magnetron sputtering discharge with Al:Zn target by ion mass spectrometry, Plasma Processes and Polymers 8 (5) (2011) 459–464. doi:10.1002/ppap.201000195.

[32] T. Welzel, S. Naumov, K. Ellmer, Ion distribution measurements to probe target and plasma processes in electronegative magnetron discharges. i. negative ions, Journal of Applied Physics 109 (7) (2011) 073302. doi:10.1063/1.3553846.

[33] S. Mahieu, W. P. Leroy, K. Van Aeken, D. Depla, Modeling the flux of high energy negative ions during reactive magnetron sputtering, Journal of Applied Physics 106 (9) (2009) 093302. doi:10.1063/1.3247545.

[34] V. Straňák, J. Blažek, S. Wrehde, P. Adámek, Z. Hubička, M. Tichý, P. Špatenka, R. Hippler, Characterization of a magnetron plasma for deposition of titanium oxide and titanium nitride films, Contributions to Plasma Physics 45 (5-6) (2005) 348–357. doi:10.1002/ctpp.200510040.

[35] S. Mráz, J. M. Schneider, Influence of the negative oxygen ions on the structure evolution of transition metal oxide thin films, Journal of Applied Physics 100 (2) (2006) 023503. doi:10.1063/1.2216354.

[36] S. Mráz, J. M. Schneider, Energy distribution of O^- ions during reactive magnetron sputtering, Applied Physics Letters 89 (5) (2006) 051502. doi:10.1063/1.2266888.

[37] P. Pokorný, J. Bulíř, J. Lančok, J. Musil, M. Novotný, Generation of positive and negative oxygen ions in magnetron discharge during reactive sputtering of alumina, Plasma Processes and Polymers 7 (11) (2010) 910–914. doi:10.1002/ppap.201000064.

[38] J.-P. Krumme, R. A. A. Hack, I. J. M. M. Raaijmakers, Energy distribution of negative O^- and OH^- ions emitted from YBaCuO and iron garnet targets by dc and rf magnetron sputtering, Journal of Applied Physics 70 (11) (1991) 6743–6756. doi:10.1063/1.349848.

[39] J.-P. Krumme, R. A. A. Hack, I. J. M. M. Raaijmakers, Energy distribution of negative oxygen ions emitted from YBaCuO and iron garnet targets by dc- and rf-magnetron sputtering, MRS Proceedings 223 (1991). doi:10.1557/proc-223-171.

[40] H. Toyoda, K. Goto, T. Ishijima, T. Morita, N. Ohshima, K. Kinoshita, Fine structure of O^- kinetic energy distribution in RF plasma and its formation mechanism, Applied Physics Express 2 (12) (2009) 126001. doi:10.1143/apex.2.126001.

[41] T. Welzel, T. Dunger, B. Liebig, F. Richter, Determination of energy modulations of negative oxygen ions during pulsed magnetron sputtering of magnesium oxide, Plasma Sources Science and Technology 20 (3) (2011) 035020. doi:10.1088/0963-0252/20/3/035020.

[42] N. Ito, N. Oka, Y. Sato, Y. Shigesato, effects of energetic ion bombardment on structural and electrical properties of Al-doped ZnO films deposited by RF-superimposed DC magnetron sputtering, Japanese Journal of Applied Physics 49 (7R) (2010) 071103. doi:10.1143/jjap.49.071103.

[43] D. Kim, J. Jang, S. Yoon, M. Hong, Effect of negative oxygen ions on a-IGZO thin films by superimposed RF/DC magnetron sputtering, ECS Transactions 64 (10) (2014) 85–91. doi:10.1149/06410.0085ecst.

[44] S. M. Rossnagel, J. J. Cuomo, Negative ion effects during magnetron and ion beam sputtering of $YBa_2Cu_3O_x$, in: AIP Conference Proceedings, Vol. 126, AIP, 1988, pp. 106–113. doi:10.1063/1.37097.

[45] L. S. Ilyinsky, B. Emmoth, E. K. Hollmann, A. G. Zaitsev, A. A. Lavrentyev,

Mass spectrometry of secondary negative ions emitted from low-energy sputtered YBCO ceramics, Journal of Physics D: Applied Physics 28 (5) (1995) 996–1000. doi:10.1088/0022-3727/28/5/022.

[46] K. Tominaga, T. Kikuma, Energetic oxygen ions in the reactive sputtering of the Zr target in Ar+O_2 atmosphere, Journal of Vacuum Science & Technology A: Vacuum, Surfaces, and Films 19 (4) (2001) 1582–1585. doi:10.1116/1.1368664.

[47] K. Tominaga, S. Iwamura, Y. Shintani, O. Tada, Energy analysis of high-energy neutral atoms in the sputtering of ZnO and $BaTiO_3$, Japanese Journal of Applied Physics 21 (5R) (1982) 688. doi:10.1143/jjap.21.688.

[48] K. Tominaga, Y. Sueyoshi, C. Munfei, Y. Shintani, Energetic O^- ions and O atoms in planar magnetron sputtering of ZnO target, Japanese Journal of Applied Physics 32 (9S) (1993) 4131. doi:10.1143/jjap.32.4131.

[49] K. Strijckmans, R. Schelfhout, D. Depla, Tutorial: Hysteresis during the reactive magnetron sputtering process, Journal of Applied Physics 124 (24) (2018) 241101. doi:10.1063/1.5042084.

[50] K. Tominaga, T. Kikuma, K. Kusaka, T. Hanabusa, Energetic oxygen ions in ZrO_2 deposition by reactive sputtering of Zr, Vacuum 66 (3-4) (2002) 279–284. doi:10.1016/s0042-207x(02)00155-0.

[51] K. Tominaga, D. Ito, Y. Miyamoto, Energetic negative ions in titanium oxide deposition by reactive sputtering in Ar/O_2, Vacuum 80 (7) (2006) 654–657. doi:10.1016/j.vacuum.2005.11.007.

[52] J. M. Andersson, E. Wallin, E. P. Münger, U. Helmersson, Energy distributions of positive and negative ions during magnetron sputtering of an Al target in Ar/O_2 mixtures, Journal of Applied Physics 100 (3) (2006) 033305. doi:10.1063/1.2219163.

[53] P. Poolcharuansin, A. Chingsungnoen, N. Pasaja, M. Horprathum, J. W. Bradley, Measurement of negative ion fluxes during DC reactive magnetron sputtering of Ti in Ar/O_2 atmosphere using a magnetic-filtering probe, Vacuum 194 (2021) 110549. doi:10.1016/j.vacuum.2021.110549.

[54] T. Suyama, H. Bae, K. Setaka, H. Ogawa, Y. Fukuoka, H. Suzuki, H. Toyoda, Quantitative evaluation of high-energy O^- ion particle flux in a DC magnetron sputter plasma with an indium-tin-oxide target, Journal of Physics D: Applied Physics 50 (44) (2017) 445201. doi:10.1088/1361-6463/aa87a1.

[55] A. L. Thomann, P. A. Cormier, V. Dolique, N. Semmar, R. Dussart, T. Lecas, B. Courtois, P. Brault, Energy transferred to the substrate surface during reactive magnetron sputtering of aluminum in Ar/O_2 atmosphere, Thin Solid Films 539 (2013) 88–95. doi:10.1016/j.tsf.2013.05.075.

[56] S. Van Steenberge, W. P. Leroy, D. Depla, Influence of oxygen flow and film thickness on the texture and microstructure of sputtered ceria thin films, Thin Solid Films 553 (2014) 2–6. doi:10.1016/j.tsf.2013.11.049.

[57] S. Van Steenberge, W. P. Leroy, A. Hubin, D. Depla, Momentum transfer driven textural changes of CeO_2 thin films, Applied Physics Letters 105 (11) (2014) 111602. doi:10.1063/1.4895785.

[58] F. Moens, T. Kalvas, S. Van Steenberge, D. Depla, Effect of space charge on the negative oxygen flux during reactive sputtering, Journal of Physics D: Applied Physics 50 (11) (2017) 115201. doi:10.1088/1361-6463/aa5ab6.

[59] H. Amemiya, T. Suzuki, Measurement of negative ions by photodetachment with YAG laser in discharge plasmas, Japanese Journal of Applied Physics 29 (9A) (1990) L1712. doi:10.1143/jjap.29.l1712.

[60] Y. Matsuda, K. Shuto, H. Nagamatsu, F. Fujiyama, Optogalvanic detection of

oxygen negative ions in reactive sputtering process, Surface and Coatings Technology 98 (1-3) (1998) 1420–1425. doi:10.1016/s0257-8972(97)00257-0.

[61] R. Dodd, S. You, J. W. Bradley, O^- density measurements in the pulsed-DC reactive magnetron sputtering of titanium, Thin Solid Films 519 (5) (2010) 1705–1711. doi:10.1016/j.tsf.2010.06.056.

[62] R. Dodd, S.-D. You, P. M. Bryant, J. W. Bradley, Negative ion density measurements in a reactive dc magnetron using the eclipse photodetachment method, Plasma Sources Science and Technology 19 (1) (2010) 015021. doi:10.1088/0963-0252/19/1/015021.

[63] S.-D. You, R. Dodd, A. Edwards, J. W. Bradley, A study of the plasma electronegativity in an argon-oxygen pulsed-dc sputter magnetron, Journal of Physics D: Applied Physics 43 (50) (2010) 505205. doi:10.1088/0022-3727/43/50/505205.

[64] S.-D. You, R. Dodd, A. Edwards, J. W. Bradley, The temporal evolution of the negative ion density in a low duty cycle pulsed reactive magnetron discharge, Surface and Coatings Technology 205 (2011) S378–S380. doi:10.1016/j.surfcoat.2011.03.145.

[65] M. Bowes, P. Poolcharuansin, J. W. Bradley, Negative ion energy distributions in reactive HiPIMS, Journal of Physics D: Applied Physics 46 (4) (2012) 045204. doi:10.1088/0022-3727/46/4/045204.

[66] S. Scribbins, M. Bowes, J. W. Bradley, The spatial distribution of negative oxygen ion densities in a dc reactive magnetron discharge, Journal of Physics D: Applied Physics 46 (4) (2012) 045203. doi:10.1088/0022-3727/46/4/045203.

[67] S. K. Karkari, C. Gaman, A. R. Ellingboe, I. Swindells, J. W. Bradley, A floating hairpin resonance probe technique for measuring time-resolved electron density in pulse discharge, Measurement Science and Technology 18 (8) (2007) 2649–2656. doi:10.1088/0957-0233/18/8/041.

[68] J. W. Bradley, R. Dodd, S.-D. You, N. S. Sirse, S. K. Karkari, Resonance hairpin and Langmuir probe-assisted laser photodetachment measurements of the negative ion density in a pulsed dc magnetron discharge, Journal of Vacuum Science & Technology A: Vacuum, Surfaces, and Films 29 (3) (2011) 031305. doi:10.1116/1.3580934.

[69] H. Amemiya, Plasmas with negative ions-probe measurements and charge equilibrium, Journal of Physics D: Applied Physics 23 (8) (1990) 999–1014. doi:10.1088/0022-3727/23/8/001.

[70] V. Straňvák, J. Blažvek, S. Wrehde, P. Adámek, Z. Hubička, M. Tichý, S. Špatenka, R. Hippler, Study of electronegative Ar/O_2 discharge by means of Langmuir probe, Contributions to Plasma Physics 48 (5-7) (2008) 503–508. doi:10.1002/ctpp.200810081.

[71] M. Bowes, J. W. Bradley, The behaviour of negative oxygen ions in the afterglow of a reactive HiPIMS discharge, Journal of Physics D: Applied Physics 47 (26) (2014) 265202. doi:10.1088/0022-3727/47/26/265202.

[72] P. Saikia, B. K. Saikia, K. S. Goswami, A. Phukan, Argon/oxygen dc magnetron discharge plasma probed with ion acoustic waves, Journal of Vacuum Science & Technology A: Vacuum, Surfaces, and Films 32 (3) (2014) 031303. doi:10.1116/1.4871081.

[73] T. E. Sheridan, P. Chabert, R. W. Boswell, Positive ion flux from a low-pressure electronegative discharge, Plasma Sources Science and Technology 8 (3) (1999) 457–462. doi:10.1088/0963-0252/8/3/316.

[74] E. Stoffels, W. W. Stoffels, V. M. Kroutilina, H.-E. Wagner, J. Meichsner, Near-surface generation of negative ions in low-pressure discharges, Journal of Vacuum

Science & Technology A: Vacuum, Surfaces, and Films 19 (5) (2001) 2109–2115. doi:10.1116/1.1374617.

[75] Y. Liu, D. W. Stracener, T. Stora, Production of negatively charged radioactive ion beams, New Journal of Physics 19 (8) (2017) 085005. doi:10.1088/1367-2630/aa609c.

[76] J. T. Gudmundsson, A critical review of the reaction set for a low pressure oxygen processing discharge, Tech. Rep. RH-17-2004, Science Institute, University of Iceland (2004).

[77] J. T. Gudmundsson, E. G. Thorsteinsson, Oxygen discharges diluted with argon: dissociation processes, Plasma Sources Science and Technology 16 (2) (2007) 399–412. doi:10.1088/0963-0252/16/2/025.

[78] A. Bogaerts, Effects of oxygen addition to argon glow discharges: a hybrid Monte Carlo-fluid modeling investigation, Spectrochimica Acta Part B: Atomic Spectroscopy 64 (11-12) (2009) 1266–1279. doi:10.1016/j.sab.2009.10.003.

[79] D. Rapp, D. D. Briglia, Total cross sections for ionization and attachment in gases by electron impact. II. Negative-ion formation, The Journal of Chemical Physics 43 (5) (1965) 1480–1489. doi:10.1063/1.1696958.

[80] Y. Itikawa, Cross sections for electron collisions with oxygen mo-lecules, Journal of Physical and Chemical Reference Data 38 (1) (2009) 1–20. doi:10.1063/1.3025886.

[81] Y. Itikawa, A. A. Ichimura, K. Onda, K. Sakimoto, K. Takayanagi, Y. Hatano, M. Hayashi, H. Nishimura, S. Tsurubuchi, Cross sections for collisions of electrons and photons with oxygen molecules, Journal of Physical and Chemical Reference Data 18 (1) (1989) 23–42. doi:10.1063/1.555841.

[82] J. T. Gudmundsson, M. A. Lieberman, Recombination rate coefficients in oxygen discharges, Tech. Rep. RH-16-2004, Science Institute, University of Iceland (2004).

[83] S. G. Belostotsky, D. J. Economou, D. V. Lopaev, T. V. Rakhimova, Negative ion destruction by $O(^3P)$ atoms and $O_2(a^1\Delta g)$ molecules in an oxygen plasma, Plasma Sources Science and Technology 14 (3) (2005) 532–542. doi:10.1088/0963-0252/14/3/016.

[84] P. D. Burrow, Dissociative attachment from the $O_2(a^1\Delta_g)$ state, Journal of Chemical Physics 59 (1973) 4922–4931. doi:10.1063/1.1680707.

[85] T. Jaffke, M. Meinke, R. Hashemi, L. G. Christophorou, E. Illenberger, Dissociative electron attachment to singlet oxygen, Chemical Physics Letters 193 (1-3) (1992) 62–68. doi:10.1016/0009-2614(92)85683-2.

[86] D. Hayashi, K. Kadota, Efficient production of O^- by dissociative attachment of slow electrons to highly excited metastable oxygen molecules, Japanese Journal of Applied Physics 38 (1R) (1999) 225. doi:10.1143/jjap.38.225.

[87] W. Trennepohl, J. Bretagne, G. Gousset, D. Pagnon, M. Touzeau, Modelling of an reactive magnetron discharge used for deposition of chromium oxide, Plasma Sources Science and Technology 5 (4) (1996) 607–621. doi:10.1088/0963-0252/5/4/002.

[88] K. Nanbu, K. Mitsui, S. Kondo, Self-consistent particle modelling of dc magnetron discharges of an O_2/Ar mixture, Journal of Physics D: Applied Physics 33 (18) (2000) 2274–2283. doi:10.1088/0022-3727/33/18/311.

[89] E. Bultinck, A. Bogaerts, Particle-in-cell/Monte Carlo collisions treatment of an Ar/O_2 magnetron discharge used for the reactive sputter deposition of TiO_x films, New Journal of Physics 11 (10) (2009) 103010. doi:10.1088/1367-2630/11/10/103010.

[90] G. D. Alton, Negative-ion formation processes and sources, in: R. Hellborg (Ed.),

Electrostatic Accelerators: Fundamentals and Applications, Springer Berlin Heidelberg, 2005, pp. 222–273. doi:10.1007/3-540-27095-7_20.

[91] M. Vasquez, D. Sasaki, T. Kasuya, S. Maeno, M. Wada, Y. Takeiri, K. Tsumori, Extraction of low-energy negative oxygen ions for thin film formation, in: AIP Conference Proceedings, Vol. 1390, AIP, 2011, pp. 692–700. doi:10.1063/1.3637442.

[92] P. Sigmund, Theory of sputtering .i. sputtering yield of amorphous and polycrystalline targets, Physical Review 184 (2) (1969) 383–416. doi:10.1103/PhysRev.184.383.

[93] K. Ohya, K. Ishida, I. Mori, Production of atomic-oxygen negative-ion beam by positive ion-induced sputtering of semiconductive $BaTiO_3$ ceramic, Japanese Journal of Applied Physics 23 (12R) (1984) 1640. doi:10.1143/jjap.23.1640.

[94] P. van der Heide, Secondary ion mass spectrometry : an introduction to principles and practices, John Wiley & Sons, Inc, 2014.

[95] M. L. Yu, Formation of molecular ions during sputtering, Physical Review B 24 (10) (1981) 5625–5633. doi:10.1103/physrevb.24.5625.

[96] M. L. Yu, Emission mechanisms of titanium oxide ions during sputtering, Physical Review B 24 (2) (1981) 1147–1150. doi:10.1103/physrevb.24.1147.

[97] M. L. Yu, The sputtering of molecular ions from surfaces in secondary ion mass spectrometry, Applications of Surface Science 11-12 (1982) 196–201. doi:10.1016/0378-5963(82)90066-6.

[98] V. E. Krohn, Emission of negative ions from metal surfaces bombarded by positive cesium ions, Journal of Applied Physics 33 (12) (1962) 3523–3525. doi:10.1063/1.1702439.

[99] K. S. Woodcock, The emission of negative ions under the bombardment of positive ions, Physical Review 38 (9) (1931) 1696–1703. doi:10.1103/physrev.38.1696.

[100] J. P. Gauyacq, A. G. Borisov, D. Teillet-Billy, Position and lifetime of atomic states close to a metal: application to resonant charge transfer, Journal of Physics: Condensed Matter 5 (33A) (1993) A269–A272. doi:10.1088/0953-8984/5/33a/091.

[101] J. K. Nørskov, B. I. Lundqvist, Secondary-ion emission probability in sputtering, Physical Review B 19 (11) (1979) 5661–5665. doi:10.1103/physrevb.19.5661.

[102] K. Wittmaack, Ion beam science : solved and unsolved problems part II, Vol. 52, Det Kongelige Danske Videnskabernes Selskab, 2006, Ch. A critical review of the electron-tunneling model of secondary ion formation, pp. 465–494.
URL http://publ.royalacademy.dk/books/162/997

[103] M. Bernheim, F. Le Bourse, On the velocity dependence for negative ionization of atoms sputtered from cesiated surfaces: An experimental study, Nuclear Instruments and Methods in Physics Research Section B: Beam Interactions with Materials and Atoms 27 (1) (1987) 94–103. doi:10.1016/0168-583x(87)90010-3.

[104] A. Wucher, Formation of atomic secondary ions in sputtering, Applied Surface Science 255 (4) (2008) 1194–1200. doi:10.1016/j.apsusc.2008.05.252.

[105] J. C. Tucek, S. G. Walton, R. L. Champion, Secondary-electron and negative-ion emission from Al: effect of oxygen coverage, Physical Review B 53 (21) (1996) 14127–14134. doi:10.1103/physrevb.53.14127.

[106] J. C. Tucek, R. L. Champion, On the dynamics of secondary-electron and anion emission from an surface, Surface Science 382 (1-3) (1997) 137–146. doi:10.1016/s0039-6028(97)00117-9.

[107] R. A. Baragiola, P. Ricardi, Reactive Sputter Deposition, Vol. 109, Springer-Verlag Berlin Heidelberg, 2008, Ch. Electron emission from surfaces induced by slow ions,

pp. 43–58.
[108] R. A. Baragiola, E. V. Alonso, J. Ferron, A. Oliva-Florio, Ion-induced electron emission from clean metals, Surface Science 90 (2) (1979) 240–255. doi:10.1016/0039-6028(79)90341-8.
[109] J. C. Tucek, S. G. Walton, R. L. Champion, Ion-induced secondary electron and negative ion emission from Mo/O, Surface Science 410 (2-3) (1998) 258–269. doi:10.1016/s0039-6028(98)00308-2.
[110] V. Zhukov, I. Popova, J. T. Yates, Initial stages of Al(111) oxidation by oxygen: Temperature and surface morphology effects, Journal of Vacuum Science & Technology A: Vacuum, Surfaces, and Films 17 (4) (1999) 1727–1732. doi:10.1116/1.581881.
[111] R. Riwan, C. Guillot, J. Paigne, Oxygen adsorption on clean Mo (100) surfaces, Surface Science 47 (1) (1975) 183–190. doi:10.1016/0039-6028(75)90284-8.
[112] S. G. Walton, R. L. Champion, Y. Wang, Negative ion emission from a stainless steel surface due to positive ion collisions, Journal of Applied Physics 84 (3) (1998) 1706–1707. doi:10.1063/1.368241.
[113] S. G. Walton, J. C. Tucek, R. L. Champion, Y. Wang, Low energy, ion-induced electron and ion emission from stainless steel: The effect of oxygen coverage and the implications for discharge modeling, Journal of Applied Physics 85 (3) (1999) 1832–1837. doi:10.1063/1.369330.
[114] W. S. Vogan, S. G. Walton, R. L. Champion, The role of O and Cl adsorbates on the secondary emission properties of tungsten, Surface Science 459 (1-2) (2000) 14–22. doi:10.1016/s0039-6028(00)00486-6.
[115] W. S. Vogan, R. L. Champion, Oxygen adsorption on a Si(100) substrate: effects on secondary emission properties, Surface Science 492 (1-2) (2001) 83–90. doi:10.1016/s0039-6028(01)01380-2.
[116] K. Wittmaack, Oxygen-concentration dependence of secondary ion yield enhancement, Surface Science 112 (1-2) (1981) 168–180. doi:10.1016/0039-6028(81)90340-x.
[117] H. Gnaser, Evidence of bond-breaking processes in sputtered ion emission, International Journal of Mass Spectrometry and Ion Processes 61 (1) (1984) 81–86. doi:10.1016/0168-1176(84)85119-8.
[118] G. Slodzian, J. F. Hennequin, Sur l'émission ionique secondaire des metaux en presence d'oxygene, Comptes rendus hebdomadaires des séances de l'académie des sciences series B 263 (22) (1966) 1246–1249.
[119] M. L. Yu, A bond breaking model for secondary ion emission, Nuclear Instruments and Methods in Physics Research Section B: Beam Interactions with Materials and Atoms 18 (1-6) (1986) 542–548. doi:10.1016/s0168-583x(86)80085-4.
[120] A. Ebanezar J., Negative ion formation in ion-molecule and ion-surface collisions, phdthesis, Ernst-Moritz-Arndt-Universität Greifswald (2014).
URL https://nbn-resolving.org/urn:nbn:de:gbv:9-002073-6
[121] P. Williams, C. A. Evans, Anomalous enhancement of negative sputtered ion emission by oxygen, Surface Science 78 (2) (1978) 324–338. doi:10.1016/0039-6028(78)90084-5.
[122] J. Lorincik, Z. Sroubek, Oxygen O18 method and the search for the ionization mechanism in sputtering of oxygenated surfaces, Applied Surface Science 255 (4) (2008) 1201–1205. doi:10.1016/j.apsusc.2008.05.072.
[123] K. Wittmaack, Aspects of quantitative secondary ion mass spectrometry, Nuclear Instruments and Methods 168 (1-3) (1980) 343–356. doi:10.1016/0029-554x(80)91275-6.

[124] K. Franzreb, J. Lörinčík, P. Williams, Quantitative study of oxygen enhancement of sputtered ion yields. I. Argon ion bombardment of a silicon surface with O_2 flood, Surface Science 573 (2) (2004) 291–309. doi:10.1016/j.susc.2004.10.001.

[125] G. R. Darling, Y. Zeiri, R. Kosloff, Charge-transfer reactions in atom scattering from ionic surfaces: a time-dependent wavepacket approach, Faraday Discussion 117 (2000) 41–54. doi:10.1039/b004003g.

[126] O. Tarvainen, R. Kronholm, M. Laitinen, M. Reponen, J. Julin, V. Toivanen, M. Napari, M. Marttinen, D. Faircloth, H. Koivisto, T. Sajavaara, Experimental evidence on photo-assisted O^- ion production from Al_2O_3 cathode in cesium sputter negative ion source, Journal of Applied Physics 128 (9) (2020) 094903. doi:10.1063/5.0020751.

[127] M. Rogala, Z. Klusek, C. Rodenbuecher, R. Waser, K. Szot, Quasi-two-dimensional conducting layer on TiO_2 (110) introduced by sputtering as a template for resistive switching, Applied Physics Letters 102 (13) (2013) 131604. doi:10.1063/1.4801437.

[128] L. M. Kishinevsky, Estimation of electron potential emission yield dependence on metal and ion parameters, Radiation Effects 19 (1) (1973) 23–27. doi:10.1080/00337577308232211.

[129] R. A. Baragiola, Electron-emission from surfaces by impact of polyatomic ions and cosmic dust, Nuclear Instruments & Methods in Physics Research Section B-Beam Interactions with Materials and Atoms 88 (1-2) (1994) 35–43. doi:10.1016/0168-583x(94)96077-1.

[130] Y. P. Raizer, Gas discharge physics, Springer, 2001.

[131] S. Mahieu, D. Depla, Correlation between electron and negative O^- ion emission during reactive sputtering of oxides, Applied Physics Letters 90 (12) (2007) 121117. doi:10.1063/1.2715113.

[132] T. Welzel, K. Ellmer, Negative oxygen ion formation in reactive magnetron sputtering processes for transparent conductive oxides, Journal of Vacuum Science & Technology A: Vacuum, Surfaces, and Films 30 (6) (2012) 061306. doi:10.1116/1.4762815.

[133] V. A. Volpyas, E. K. Hollmann, D. A. Plotkin, V. I. Goldrin, Ion plasma sputtering of multi-component materials, Vacuum 51 (2) (1998) 227–230. doi:10.1016/s0042-207x(98)00164-x.

[134] H. Li, K. Karahashi, M. Fukasawa, K. Nagahata, T. Tatsumi, S. Hamaguchi, Sputtering yields and surface chemical modification of tin-doped indium oxide in hydrocarbon-based plasma etching, Journal of Vacuum Science & Technology A: Vacuum, Surfaces, and Films 33 (6) (2015) 060606. doi:10.1116/1.4927125.

[135] D. R. Baer, M. H. Engelhard, A. S. Lea, P. Nachimuthu, T. C. Droubay, J. Kim, B. Lee, C. Mathews, R. L. Opila, L. V. Saraf, W. F. Stickle, R. M. Wallace, B. S. Wright, Comparison of the sputter rates of oxide films relative to the sputter rate of SiO_2, Journal of Vacuum Science & Technology A 28 (5) (2010) 1060–1072. doi:10.1116/1.3456123.

[136] D. Depla, S. Mahieu, R. De Gryse, Magnetron sputter deposition: Linking discharge voltage with target properties, Thin Solid Films 517 (9) (2009) 2825–2839. doi:10.1016/j.tsf.2008.11.108.

[137] S. D. Nehate, A. Prakash, P. D. Mani, K. B. Sundaram, Work function extraction of indium tin oxide films from MOSFET devices, ECS Journal of Solid State Science and Technology 7 (3) (2018) P87–P90. doi:10.1149/2.0081803jss.

[138] Y. Takeishi, Ejection of electrons from barium oxide by noble gas ions, Journal of

the Physical Society of Japan 17 (2) (1962) 326–341. doi:10.1143/jpsj.17.326.
[139] H. Uchiike, K. Sekiya, T. Hashimoto, T. Shinoda, Y. Fukushima, Optimum composition of CaO, SrO dielectric materials in AC plasma display panels, IEEE Transactions on Electron Devices 30 (12) (1983) 1735–1742. doi:10.1109/t-ed.1983.21438.
[140] S. Yoshimura, K. Hine, M. Kiuchi, J. Hashimoto, M. Terauchi, Y. Honda, M. Nishitani, S. Hamaguchi, Sputtering yields of CaO, SrO, and BaO by monochromatic noble gas ion bombardment, Japanese Journal of Applied Physics 51 (8S1) (2012) 08HB02. doi:10.1143/jjap.51.08hb02.
[141] A. Benninghoven, L. Wiedmann, Investigation of surface reactions by the static method of secondary ion mass spectrometry, Surface Science 41 (2) (1974) 483–492. doi:10.1016/0039-6028(74)90064-8.
[142] A. Müller, A. Benninghoven, Investigation of surface reactions by the static method of secondary ion mass spectrometry, Surface Science 41 (2) (1974) 493–503. doi:10.1016/0039-6028(74)90065-x.
[143] A. Benninghoven, A. A. Müller, Investigation of surface reactions by the static method of secondary ion mass spectrometry, Surface Science 39 (2) (1973) 416–426. doi:10.1016/0039-6028(73)90012-5.
[144] A. Müller, A. A. Benninghoven, Investigation of surface reactions by the static method of secondary ion mass spectrometry, Surface Science 39 (2) (1973) 427–436. doi:10.1016/0039-6028(73)90013-7.
[145] Y. Shintani, K. Nakanishi, T. Takawaki, O. Tada, Behaviours of high-energy electrons and neutral atoms in the sputtering of $BaTiO_3$, Japanese Journal of Applied Physics 14 (12) (1975) 1875–1879. doi:10.1143/jjap.14.1875.
[146] K. Ellmer, T. Welzel, Reactive magnetron sputtering of transparent conductive oxide thin films: Role of energetic particle (ion) bombardment, Journal of Materials Research 27 (5) (2012) 765–779. doi:10.1557/jmr.2011.428.
[147] K. Berndt, B. Rammelt, S. C. W. Heichler, Auger depth profiling of $BaTiO_3$ ceramics, Crystal Research and Technology 25 (10) (1990) 1211–1217. doi:10.1002/crat.2170251019.
[148] R. Schelfhout, K. Strijckmans, D. Depla, Sputter yield measurements to evaluate the target state during reactive magnetron sputtering, Surface and Coatings Technology 399 (2020) 126097. doi:10.1016/j.surfcoat.2020.126097.
[149] N. Brenning, J. T. Gudmundsson, D. Lundin, T. Minea, M. A. Raadu, U. Helmersson, The role of Ohmic heating in dc magnetron sputtering, Plasma Sources Science and Technology 25 (2016) 065024. doi:10.1088/0963-0252/25/6/065024.
[150] K. Van Aeken, S. Mahieu, D. Depla, The metal flux from a rotating cylindrical magnetron: a monte carlo simulation, Journal of Physics D-Applied Physics 41 (20) (2008) 205307. doi:10.1088/0022-3727/41/20/205307.
[151] D. Depla, W. P. Leroy, Magnetron sputter deposition as visualized by monte carlo modeling, Thin Solid Films 520 (20) (2012) 6337–6354. doi:10.1016/j.tsf.2012.06.032.
[152] C. Salinga, H. Weis, M. Wuttig, Gasochromic switching of tungsten oxide films: a correlation between film properties and coloration kinetics, Thin Solid Films 414 (2) (2002) 288–295. doi:10.1016/s0040-6090(02)00496-0.
[153] D. Severin, O. Kappertz, T. Nyberg, S. Berg, M. Wuttig, The effect of target aging on the structure formation of zinc oxide during reactive sputtering, Thin Solid Films 515 (7-8) (2007) 3554–3558. doi:10.1016/j.tsf.2006.10.130.
[154] T. Welzel, K. Ellmer, The influence of the target age on laterally resolved ion distributions in reactive planar magnetron sputtering, Surface and Coatings Tech-

nology 205 (2011) S294–S298. doi:10.1016/j.surfcoat.2011.01.050.

[155] D. Depla, K. Strijckmans, R. De Gryse, The role of the erosion groove during reactive sputter deposition, Surface & Coatings Technology 258 (2014) 1011–1015. doi:10.1016/j.surfcoat.2014.07.038.

[156] F. Boydens, W. P. Leroy, R. Persoons, D. Depla, The influence of target surface morphology on the deposition flux during direct-current magnetron sputtering, Thin Solid Films 531 (2013) 32–41. doi:10.1016/j.tsf.2012.11.097.

[157] A. Bikowski, T. Welzel, K. Ellmer, The correlation between the radial distribution of high-energetic ions and the structural as well as electrical properties of magnetron sputtered ZnO:al films, Journal of Applied Physics 114 (22) (2013) 223716. doi:10.1063/1.4840975.

[158] R. De Gryse, J. Haemers, W. P. Leroy, D. Depla, Thirty years of rotatable magnetrons, Thin Solid Films 520 (18) (2012) 5833–5845. doi:10.1016/j.tsf.2012.04.065.

[159] V. Sittinger, A. Pflug, C. Schulz, M. Siemers, T. Melzig, B. Meyer, A. Kronenberger, J. Oberste Berghaus, W. De Bosscher, Growth condition of amorphous ZTO films from rotatable targets, Surface and Coatings Technology 267 (2015) 75–80. doi:10.1016/j.surfcoat.2014.12.014.

[160] R. Tonneau, P. Moskovkin, J. Muller, T. Melzig, E. Haye, S. Konstantinidis, A. Pflug, S. Lucas, Understanding the role of energetic particles during the growth of TiO_2 thin films by reactive magnetron sputtering through multi-scale Monte Carlo[160] simulations and experimental deposition, Journal of Physics D: Applied Physics 54 (15) (2021) 155203. doi:10.1088/1361-6463/abd72a.

[161] D. Depla, G. Buyle, J. Haemers, R. De Gryse, Discharge voltage measurements during magnetron sputtering, Surface and Coatings Technology 200 (14-15) (2006) 4329–4338. doi:10.1016/j.surfcoat.2005.02.166.

[162] D. Depla, J. Haemers, R. De Gryse, Influencing the hysteresis during reactive magnetron sputtering by gas separation, Surface & Coatings Technology 235 (2013) 62–67. doi:10.1016/j.surfcoat.2013.07.012.

[163] J. M. E. Harper, J. J. Cuomo, R. J. Gambino, H. R. Kaufman, R. S. Robinson, Mean free path of negative ions in diode sputtering, Journal of Vacuum Science and Technology 15 (4) (1978) 1597–1600. doi:10.1116/1.569816.

[164] J. M. E. Harper, J. J. Cuomo, R. J. Gambino, H. R. Kaufman, R. S. Robinson, Erratum: Mean free path of negative ions in diode sputtering [J.Vac.Sci. Technol. 15, 1597 (1978)], Journal of Vacuum Science and Technology 18 (1) (1981) 112–112. doi:10.1116/1.570687.

[165] T. I. Selinder, G. Larsson, U. Helmersson, S. Rudner, Resputtering effects on the stoichiometry of $YBa_2Cu_3O_x$ thin films, Journal of Applied Physics 69 (1) (1991) 390–395. doi:10.1063/1.347727.

[166] S. M. Rossnagel, H. R. Kaufman, Charge transport in magnetrons, Journal of Vacuum Science & Technology A: Vacuum, Surfaces, and Films 5 (4) (1987) 2276–2279. doi:10.1116/1.574434.

[167] B. B. Sahu, L. Wen, J. H. Kwon, J. G. Han, Factors affecting the properties of highly conductive flexible ultrathin ITO films in confined large area magnetron sputtering in three dimensions, AIP Advances 8 (10) (2018) 105112. doi:10.1063/1.5053570.

[168] B. B. Sahu, L. Wen, S. H. Kim, J. G. Han, Study of plasma characteristic and properties of flexible ultra-thin ITO films prepared by large area 3-D confined and planar magnetron sputtering, Vacuum 165 (2019) 246–253. doi:10.1016/j.vacuum.2019.04.029.

[169] W. Kautek, Deposition methods of high-Tc superconductors, Vacuum 43 (5-7) (1992) 403–411. doi:10.1016/0042-207x(92)90045-x.

[170] P. G. Quigley, R. A. Rao, C. B. Eom, Time dependence and spatial distribution of the deposition rate of $YBa_2Cu_3O_7$ thin films in 90° off-axis sputtering, Journal of Vacuum Science & Technology A: Vacuum, Surfaces, and Films 15 (6) (1997) 2854–2858. doi:10.1116/1.580839.

[171] M. S. Raven, Radio frequency sputtering and the deposition of high-temperature superconductors, Journal of Materials Science Materials in Electronics 5 (3) (1994) 129–146. doi:10.1007/bf01198944.

[172] H. Takeda, Y. Sato, Y. Yoshinori Iwabuchi, M. Yoshikawa, Y. Shigesato, Electrical and optical properties of Al-doped ZnO films deposited by hollow cathode gas flow sputtering, Thin Solid Films 517 (10) (2009) 3048–3052. doi:10.1016/j.tsf.2008.11.114.

[173] O. Michikami, M. Asahi, YBaCuO epitaxial film formation by magnetron sputtering with facing targets I. Effects of target and substrate positions, Japanese Journal of Applied Physics 30 (5R) (1991) 939. doi:10.1143/jjap.30.939.

[174] J.-H. Xu, G.-G. Zheng, A. M. Grishin, B. M. Moon, K. V. Rao, J. Moreland, Novel $YBa_2Cu_3O_{7\text{-}x}$ and $YBa_2Cu_3O_{7\text{-}x}/Y_4Ba_3O_9$ multilayer films by bias-masked "on-axis" magnetron sputtering, Applied Physics Letters 64 (14) (1994) 1874–1876. doi:10.1063/1.111784.

[175] J.-H. Xu, B. M. Moon, K. V. Rao, Study of the resputtering effect during rf-sputter depositionof YBCO films, Journal of Materials Research 10 (4) (1995) 798–802. doi:10.1557/JMR.1995.0798.

[176] Y. Hoshi, H. Kato, K. Funatsu, Structure and electrical properties of ITO thin films deposited at high rate by facing target sputtering, Thin Solid Films 445 (2) (2003) 245–250. doi:10.1016/s0040-6090(03)01182-9.

[177] H. Lei, K. Ichikawa, M. Wang, Y. Hoshi, T. Uchida, Y. Sawada, Investigation of low-damage sputter-deposition of ITO films on organic emission layer, IEICE Transactions on Electronics E91-C (10) (2008) 1658–1662. doi:10.1093/ietele/e91-c.10.1658.

[178] H. Lei, K. Ichikawa, Y. Hoshi, M. Wang, T. Uchida, Y. Sawada, A study of deposition of ITO films on organic layer using facing target sputtering in Ar and Kr gases, Thin Solid Films 518 (11) (2010) 2926–2929. doi:10.1016/j.tsf.2009.08.059.

[179] Y. Yasuda, Y. Hoshi, S. Kobayashi, T. Uchida, Y. Sawada, M. Wang, H. Lei, Reactive sputter deposition of WO_3 films by using two deposition methods, Journal of Vacuum Science & Technology A 37 (3) (2019) 031514. doi:10.1116/1.5092863.

[180] F. Fumagalli, J. Martí-Rujas, F. Di Fonzo, Room temperature deposition of high figure of merit Al-doped zinc oxide by pulsed-direct current magnetron sputtering: Influence of energetic negative ion bombardment on film's optoelectronic properties, Thin Solid Films 569 (2014) 44–51. doi:10.1016/j.tsf.2014.08.023.

[181] J. Jia, A. Yoshimura, Y. Kagoya, N. Oka, Y. Shigesato, Transparent conductive Al and Ga doped ZnO films deposited using off-axis sputtering, Thin Solid Films 559 (2014) 69–77. doi:10.1016/j.tsf.2014.02.005.

[182] W.-J. Lee, D.-H. Cho, J.-H. Wi, W. S. Han, B.-K. Kim, S. D. Choi, J.-Y. Baek, Y. D. Chung, Characterization of bilayer AZO film grown by low-damage sputtering for $Cu(In,Ga)Se_2$ solar cell with a CBD-ZnS buffer layer, Materials Science in Semiconductor Processing 81 (2018) 48–53. doi:10.1016/j.mssp.2018.03.008.

[183] L. W. Rieth, P. H. Holloway, Influence of negative ion resputtering on ZnO:Al thin films, Journal of Vacuum Science & Technology A: Vacuum, Surfaces, and

Films 22 (1) (2004) 20–29. doi:10.1116/1.1626641.
[184] S.-M. Nam, T. Tsurumi, In situ epitaxial growth of lead zirconate titanate films by bias sputtering at high RF power, Japanese Journal of Applied Physics 43 (5R) (2004) 2672. doi:10.1143/jjap.43.2672.
[185] J. N. Jang, Y. J. Lee, Y. Jang, J. Yun, S. Yi, M. Hong, Post-annealing-free, room temperature processed nanocrystalline indium tin oxide thin films for plastic electronics, Journal of Physics D: Applied Physics 49 (21) (2016) 215303. doi:10.1088/0022-3727/49/21/215303.
[186] E. Aydin, C. Altinkaya, Y. Smirnov, M. A. Yaqin, K. P. S. Zanoni, A. Paliwal, Y. Firdaus, T. G. Allen, T. D. Anthopoulos, H. J. Bolink, M. Morales-Masis, S. De Wolf, Sputtered transparent electrodes for optoelectronic devices: Induced damage and mitigation strategies, Matter 4 (11) (2021) 3549–3584. doi:10.1016/j.matt.2021.09.021.
[187] R. E. Williford, R. Devanathan, W. J. Weber, Computer simulation of displacement energies for several ceramic materials, Nuclear Instruments and Methods in Physics Research Section B: Beam Interactions with Materials and Atoms 141 (1-4) (1998) 94–98. doi:10.1016/s0168-583x(98)00066-4.
[188] S. J. Zinkle, C. Kinoshita, Defect production in ceramics, Journal of Nuclear Materials 251 (1997) 200–217. doi:10.1016/s0022-3115(97)00224-9.
[189] A. Anders, A structure zone diagram including plasma-based deposition and ion etching, Thin Solid Films 518 (15) (2010) 4087–4090. doi:10.1016/j.tsf.2009.10.145.
[190] K. Tominaga, M. Chong, Y. Shintani, Energetic particles in the sputtering of an indium–tin oxide target, Journal of Vacuum Science & Technology A: Vacuum, Surfaces, and Films 12 (4) (1994) 1435–1438. doi:10.1116/1.579333.
[191] M. T. Greiner, L. Chai, M. G. Helander, W.-M. Tang, Z.-H. Lu, Transition metal oxide work functions: The influence of cation oxidation state and oxygen vacancies, Advanced Functional Materials 22 (21) (2012) 4557–4568. doi:10.1002/adfm.201200615.
[192] V. Crist, Private Communication (2018).
[193] M. A. Sobolewski, In situ measurement of electron emission yield at silicon dioxide surfaces exposed to argon plasmas, Plasma Sources Science and Technology 30 (2) (2021) 025004. doi:10.1088/1361-6595/abd61f.
[194] H. Li, K. Karahashi, M. Fukasawa, K. Nagahata, T. Tatsumi, S. Hamaguchi, Mass-selected ion beam study on etching characteristics of ZnO by methane-based plasma, Japanese Journal of Applied Physics 55 (2) (2016) 021202. doi:10.7567/jjap.55.021202.
[195] S. Xiao, F. Feng, K. Shi, S. Deng, T. Qu, Y. Zhu, H. Lu, R. Huang, Z. Han, Resputtering effect during MgO buffer layer deposition by magnetron sputtering for superconducting coated conductors, Journal of Vacuum Science & Technology A: Vacuum, Surfaces, and Films 33 (4) (2015) 041504. doi:10.1116/1.4921198.
[196] S. Z. Xiao, F. Feng, T. M. Qu, H. Y. Lu, X. S. Zhang, Z. H. Han, A method to fabricate biaxially textured MgO buffer layer for HTS coated conductor, IEEE transactions on applied superconductivity 26 (3) (2016) 7500805. doi:10.1109/TASC.2016.2532960.
[197] S. Mahieu, D. Depla, Reactive sputter deposition of TiN layers: modelling the growth by characterization of particle fluxes towards the substrate, Journal of Physics D: Applied Physics 42 (5) (2009) 053002. doi:10.1088/0022-3727/42/5/053002.
[198] S. Vyas, Simulation of ceria: : bulk and surface defects, phdthesis, University of

London (1997).
[199] P. Maldonado, J. R. A. Godinho, L. Z. Evins, P. M. Oppeneer, Ab initio prediction of surface stability of fluorite materials and experimental verification, The Journal of Physical Chemistry C 117 (13) (2013) 6639–6650. doi:10.1021/jp312645f.
[200] B. Braeckman, Sputter deposition of TiAlN (in Dutch), mathesis, Ghent University (2012).
URL https://lib.ugent.be/fulltxt/RUG01/001/886/972/RUG01-001886972_2012_0001_AC.pdf
[201] K. G. Ressler, N. Sonnenberg, M. J. Cima, Mechanism of biaxial alignment of oxide thin films during ion-beam-assisted deposition, Journal of the American Ceramic Society 80 (10) (2005) 2637–2648. doi:10.1111/j.1151-2916.1997.tb03166.x.
[202] L. Dong, D. J. Srolovitz, Mechanism of texture development in ion-beam-assisted deposition, Applied Physics Letters 75 (4) (1999) 584–586. doi:10.1063/1.124449.
[203] J. E. Mahan, A. Vantomme, A simplified collisional model of sputtering in the linear cascade regime, Journal of Vacuum Science & Technology a-Vacuum Surfaces and Films 15 (4) (1997) 1976–1989. doi:10.1116/1.580668.
[204] A. A. Ivanova, Hydroxyapatite-based coatings deposited by radio frequency magnetron sputtering, Thesis, National Research Tomsk Polytechnic University (2017).
[205] J. M. Ngaruiya, O. Kappertz, S. H. Mohamed, M. Wuttig, Structure formation upon reactive direct current magnetron sputteringof transition metal oxide films, Applied Physics Letters 85 (5) (2004) 748–750. doi:10.1063/1.1777412.
[206] A. Amin, D. Köhl, M. Wuttig, The role of energetic ion bombardment during growth of TiO_2 thin films by reactive sputtering, Journal of Physics D: Applied Physics 43 (40) (2010) 405303. doi:10.1088/0022-3727/43/40/405303.
[207] K. Tominaga, N. Ueshiba, Y. Shintani, O. Tada, High-energy neutral atoms in the sputtering of ZnO, Japanese Journal of Applied Physics 20 (3) (1981) 519. doi:10.1143/jjap.20.519.
[208] S. B. Krupanidhi, M. Sayer, Position and pressure effects in rf magnetron reactive sputter deposition of piezoelectric zinc oxide, Journal of Applied Physics 56 (11) (1984) 3308–3318. doi:10.1063/1.333895.
[209] I. Petrov, V. Orlinov, A. Misiuk, Highly oriented ZnO films obtained by d.c. reactive sputtering of a zinc target, Thin Solid Films 120 (1) (1984) 55–67. doi:10.1016/0040-6090(84)90173-1.
[210] Y. E. Lee, D. B. Lee, Y. J. Kim, H. K. Yang, J. C. Park, H. J. Kim, Microstructural evolution and preferred orientation change of radio-frequency-magnetron sputtered ZnO thin films, Journal of Vacuum Science & Technology A: Vacuum, Surfaces, and Films 14 (3) (1996) 1943–1948. doi:10.1116/1.580365.
[211] K. B. Sundaram, A. Khan, Characterization and optimization of zinc oxide films by r.f. magnetron sputtering, Thin Solid Films 295 (1-2) (1997) 87–91. doi:10.1016/s0040-6090(96)09274-7.
[212] V. Bhavanasi, C. B. Singh, D. Datta, V. Singh, K. Shahi, S. Kumar, Structural, optical and light scattering properties of post etched RF sputtered ZnO:al thin films deposited at various substrate temperature, Optical Materials 35 (7) (2013) 1352–1359. doi:10.1016/j.optmat.2013.01.037.
[213] T. Yanagitani, S. Tomohiro, T. Nohara, M. Matsukawa, Y. Watanabe, T. Otani, Characterization of $(11\bar{2}0)$ textured ZnO films fabricated by RF magnetron sputtering, Japanese Journal of Applied Physics 43 (5S) (2004) 3004. doi:

10.1143/jjap.43.3004.

[214] S. Takayanagi, T. Yanagitani, M. Matsukawa, Unusual growth of polycrystalline oxide film induced by negative ion bombardment in the capacitively coupled plasma deposition, Applied Physics Letters 101 (23) (2012) 232902. doi:10.1063/1.4769224.

[215] P. Sharma, K. Sreenivas, K. V. Rao, Analysis of ultraviolet photoconductivity in ZnO films prepared by unbalanced magnetron sputtering, Journal of Applied Physics 93 (7) (2003) 3963–3970. doi:10.1063/1.1558994.

[216] T. Hada, K. Wasa, S. Hayakawa, Structures and electrical properties of zinc oxide films prepared by low pressure sputtering system, Thin Solid Films 7 (2) (1971) 135–145. doi:10.1016/0040-6090(71)90032-0.

[217] N. Fujimura, T. Nishihara, S. Goto, J. Xu, T. Ito, Control of preferred orientation for ZnO films: control of self-texture, Journal of Crystal Growth 130 (1-2) (1993) 269–279. doi:10.1016/0022-0248(93)90861-p.

[218] K. Tominaga, Y. Sueyoshi, H. Imai, M. Shirai, Influence of energetic particles on ZnO films in the preparation by planar magnetron sputtering with obliquely facing targets, Japanese Journal of Applied Physics 31 (9S) (1992) 3009. doi:10.1143/jjap.31.3009.

[219] M. Minakata, N. Chubachi, Y. Kikuchi, Variation of c-axis orientation of ZnO thin films deposited by DC diode sputtering, Japanese Journal of Applied Physics 12 (3) (1973) 474–475. doi:10.1143/jjap.12.474.

[220] D. Köhl, The influence of energetic bombardment on the structure formation of sputtered zinc oxide films : development of an atomistic growth model and its application to tailor thin film properties, phdthesis, RTWH Aachen (2011). URL https://publications.rwth-aachen.de/record/64301

[221] B. Belmekki, M. S. Raven, Superlattice formation and faulted structures in r.f.-sputtered ZnO, Philosophical Magazine A 52 (1) (1985) 19–27. doi:10.1080/01418618508237602.

[222] D. Köhl, M. Luysberg, M. Wuttig, Highly textured zinc oxide films by room temperature ion beam assisted deposition, physica status solidi (RRL) - Rapid Research Letters 3 (7-8) (2009) 236–238. doi:10.1002/pssr.200903228.

[223] D. Köhl, G. Natarajan, M. Wuttig, Structure control of sputtered zinc oxide films by utilizing zinc oxide seed layers tailored by ion beam assisted sputtering, Journal of Physics D: Applied Physics 45 (24) (2012) 245302. doi:10.1088/0022-3727/45/24/245302.

[224] A. Sulyok, M. Menyhard, J. B. Malherbe, Stability of ZnO{0001} against low energy ion bombardment, Surface Science 601 (8) (2007) 1857–1861. doi:10.1016/j.susc.2007.02.011.

[225] N. F. Foster, Crystallographic orientation of zinc oxide films deposited by triode sputtering, Journal of Vacuum Science and Technology 6 (1) (1969) 111–114. doi:10.1116/1.1492638.

[226] Y. E. Lee, Y. J. Kim, H. J. Kim, Thickness dependence of microstructural evolution of ZnO films deposited by rf magnetron sputtering, Journal of Materials Research 13 (5) (1998) 1260–1265. doi:10.1557/jmr.1998.0180.

[227] T. A. Jennings, W. McNeill, Sputtering due to negative ions in oxygen discharges, Applied Physics Letters 12 (2) (1968) 25–26. doi:10.1063/1.1651877.

[228] K. Norrman, P. Norby, E. Stamate, Preferential zinc sputtering during the growth of aluminum doped zinc oxide thin films by radio frequency magnetron sputtering, Journal of Materials Chemistry C 10 (39) (2022) 14444–14452. doi:10.1039/d2tc02180c.

[229] D. J. Kester, R. Messier, Macro-effects of resputtering due to negative ion bombardment of growing thin films, Journal of Materials Research 8 (8) (1993) 1928–1937. doi:10.1557/jmr.1993.1928.

[230] Y. Saito, K. Sakabe, K. Ishihara, K. Manaka, S. Suganomata, Preparation of Y-Ba-Cu-O films by dc sputtering, Japanese Journal of Applied Physics 27 (6R) (1988) 1103. doi:10.1143/jjap.27.1103.

[231] J. J. Hanak, J. P. Pellicane, Effect of secondary electrons and negative ions on sputtering of films, Journal of Vacuum Science and Technology 13 (1) (1976) 406–409. doi:10.1116/1.568931.

[232] J. M. Grace, D. B. McDonald, M. T. Reiten, J. Olson, R. T. Kampwirth, K. E. Gray, Selective resputtering of bismuth in sputtered Bi-Sr-Ca-Cu-O films, Journal of Applied Physics 70 (7) (1991) 3867–3875. doi:10.1063/1.349193.

[233] J. M. Grace, D. B. McDonald, M. T. Reiten, J. Olson, R. T. Kampwirth, K. E. Gray, Effect of oxidant on resputtering of Bi from Bi-Sr-Ca-Cu-O films, Journal of Vacuum Science & Technology A: Vacuum, Surfaces, and Films 10 (4) (1992) 1600–1603. doi:10.1116/1.578051.

[234] K. Hirata, K. Ishibashi, N. Hosokawa, Study of the sputtering of one-, two- and three-component targets for the preparation of $YBa_2Cu_3O_7$ superconducting film, Thin Solid Films 206 (1-2) (1991) 132–136. doi:10.1016/0040-6090(91)90407-o.

[235] M. Kumar, N. D. Kataria, V. S. Tomar, V. N. Ojha, N. Khare, S. U. M. Rao, G. S. N. Reddy, A. K. Gupta, Thin films of Y-Ba-Cu-O by rf sputtering and study of Josephson effect, Bulletin of Materials Science 14 (2) (Kumar1991) 461–467. doi:10.1007/bf02747357.

[236] B. Feddes, J. G. C. Wolke, J. A. Jansen, A. M. Vredenberg, Radio frequency magnetron sputtering deposition of calcium phosphate coatings: Monte Carlo simulations of the deposition process and depositions through an aperture, Journal of Applied Physics 93 (1) (2003) 662–670. doi:10.1063/1.1525857.

[237] P. D. Rack, M. D. Potter, A. Woodard, S. Kurinec, Negative ion resputtering in $Ta_2Zn_3O_8$ thin films, Journal of Vacuum Science &Technology A: Vacuum, Surfaces, and Films 17 (5) (1999) 2805–2810. doi:10.1116/1.581947.

[238] Y. Cai, W. Liu, Q. He, Y. Zhang, T. Yu, Y. Sun, Influence of negative ion resputtering on Al-doped ZnO thin films prepared bymid-frequency magnetron sputtering, Applied Surface Science 256 (2010) 1694–1679. doi:10.1016/j.apsusc.2009.09.096.

[239] L. Zhang, T. T. Tan, S. Li, The effects of composition deviations on the microstructure and thermoelectric performance of $Ca_3Co_4O_9$ thin film, Journal of Materials Science: Materials in Electronics 29 (15) (2018) 13321–13327. doi:10.1007/s10854-018-9456-7.

[240] D. J. Kester, R. Messier, Micro-effects of resputtering due to negative ion bombardment of growing thin films, Journal of Materials Research 8 (8) (1993) 1938–1957. doi:10.1557/jmr.1993.1938.

[241] A. H. Youssef, F. A. Vargas, I. Amaechi, A. Sarkissian, A. Merlen, R. Thomas, A. Ruediger, Impact of negative oxygen ions on the deposition processes of RF-magnetron sputtered $SrTiO_3$ thin films, Thin Solid Films 661 (2018) 23–31. doi:10.1016/j.tsf.2018.05.054.

[242] M. Macias-Montero, F. J. Garcia-Garcia, R. Álvarez, J. Gil-Rostra, J. C. González, J. Cotrino, A. R. Gonzalez-Elipe, A. Palmero, Influence of plasma-generated negative oxygen ion impingement on magnetron sputtered amorphous SiO_2 thin films during growth at low temperatures, Journal of Applied Physics 111 (5) (2012)

054312. doi:10.1063/1.3691950.
[243] C. May, J. Strümpfel, ITO coating by reactive magnetron sputtering-comparison of properties from DC and MF processing, Thin Solid Films 351 (1-2) (1999) 48–52. doi:10.1016/s0040-6090(99)00206-0.
[244] X. B. Zhang, Z. L. Pei, J. Gong, C. Sun, Investigation on the electrical properties and inhomogeneous distribution of ZnO:Al thin films prepared by dc magnetron sputtering at low deposition temperature, Journal of Applied Physics 101 (1) (2007) 014910. doi:10.1063/1.2407265.
[245] D. Song, P. Widenborg, W. Chin, A. G. Aberle, Investigation of lateral parameter variations of Al-doped zinc oxide films prepared on glass substrates by rf magnetron sputtering, Solar Energy Materials and Solar Cells 73 (1) (2002) 1–20. doi:10.1016/s0927-0248(01)00104-0.
[246] H. C. Nguyen, T. T. Trinh, T. Le, C. V. Tran, T. Tran, H. Park, V. A. Dao, J. Yi, The mechanisms of negative oxygen ion formation from Al-doped ZnO target and the improvements in electrical and optical properties of thin films using off-axis dc magnetron sputtering at low temperature, Semiconductor Science and Technology 26 (10) (2011) 105022. doi:10.1088/0268-1242/26/10/105022.
[247] C. Hao, B. Xie, M. Li, H. Wang, Y. Jiang, Y. Song, The influences of high energetic oxygen negative ions and active oxygen on the microstructure and electrical properties of ZnO:al films by MF magnetron sputtering, Applied Surface Science 258 (20) (2012) 8234–8240. doi:10.1016/j.apsusc.2012.05.027.
[248] W. Dewald, V. V. Sittinger, W. Werner, C. Jacobs, B. Szyszka, Optimization of process parameters for sputtering of ceramic ZnO:Al_2O_3 targets for a-Si:H/μc-Si:H solar cells, Thin Solid Films 518 (4) (2009) 1085–1090. doi:10.1016/j.tsf.2009.04.068.
[249] D. Herrmann, M. Oertel, R. Menner, M. Powalla, Analysis of relevant plasma parameters for ZnO:Al film deposition based on data from reactive and non-reactive DC magnetron sputtering, Surface and Coatings Technology 174-175 (2003) 229–234. doi:10.1016/s0257-8972(03)00524-3.
[250] O. Kluth, G. Schöpe, B. Rech, R. Menner, M. Oertel, K. Orgassa, H. W. Schock, Comparative material study on RF and DC magnetron sputtered ZnO:al films, Thin Solid Films 502 (1-2) (2006) 311–316. doi:10.1016/j.tsf.2005.07.313.
[251] A. Bikowski, K. Ellmer, Influence of the deposition temperature on electronic transport and structural properties of radio frequency magnetron-sputtered $Zn_{1\text{-}x}Mg_xO$:Al and ZnO:Al films, Journal of Materials Research 27 (17) (2012) 2249–2256. doi:10.1557/jmr.2012.113.
[252] W. L. Patterson, G. A. Shirn, The sputtering of nickel–chromium alloys, Journal of Vacuum Science and Technology 4 (6) (1967) 343–346. doi:10.1116/1.1492560.
[253] D. Horwat, M. Jullien, F. Capon, J.-F. Pierson, J. Andersson, J. L. Endrino, On the deactivation of the dopant and electronic structure in reactively sputtered transparent Al-doped ZnO thin films, Journal of Physics D: Applied Physics 43 (13) (2010) 132003. doi:10.1088/0022-3727/43/13/132003.
[254] D. Kim, S. Yoon, M. Hong, Effects of the bombardment of negative oxygen ions on gate bias stability of InGaZnO thin film transistors, ECS Transactions 64 (10) (2014) 79–83. doi:10.1149/06410.0079ecst.
[255] D. Kim, J. Jang, S. Yoon, M. Hong, Effects of bombardment of negative oxygen ions on amorphous indium gallium zinc oxide thin films by superimposed rf/dc magnetron sputtering, Applied Physics Express 7 (3) (2014) 031401. doi:10.7567/apex.7.031401.
[256] T. Minami, J. Oda, J. Nomoto, T. Miyata, Effect of target properties on trans-

parent conducting impurity-doped ZnO thin films deposited by DC magnetron sputtering, Thin Solid Films 519 (1) (2010) 385–390. doi:10.1016/j.tsf.2010.08.007.

[257] T. Minami, O. Ohtani, T. Miyata, T. Kuboi, Transparent conducting Al-doped ZnO thin films prepared by magnetron sputtering with dc and rf powers applied in combination, Journal of Vacuum Science & Technology A: Vacuum, Surfaces, and Films 25 (4) (2007) 1172–1177. doi:10.1116/1.2748809.

[258] A. Bikowski, T. Welzel, K. Ellmer, The impact of negative oxygen ion bombardment on electronic and structural properties of magnetron sputtered ZnO:al films, Applied Physics Letters 102 (24) (2013) 242106. doi:10.1063/1.4811647.

[259] F. Meng, S. Peng, G. Xu, Y. Wang, F. Ge, F. Huang, Optimizing the discharge voltage in magnetron sputter deposition of high quality Al-doped ZnO thin films, Journal of Vacuum Science & Technology A: Vacuum, Surfaces, and Films 33 (6) (2015) 061503. doi:10.1116/1.4927437.

[260] F. Meng, F. Ge, Y. Chen, G. Xu, F. Huang, Local structural changes induced by ion bombardment in magnetron sputtered ZnO: Al films: Raman, XPS, and XAS study, Surface and Coatings Technology 365 (2019) 2–9. doi:10.1016/j.surfcoat.2018.04.013.

[261] F. Meng, S. Peng, G. Xu, Y. Wang, F. Ge, F. Huang, Structure of uniform and high-quality Al-doped ZnO films by magnetron sputter deposition at low temperatures, Thin Solid Films 665 (2018) 109–116. doi:10.1016/j.tsf.2018.08.047.

[262] D. R. Locker, J. M. Meese, Displacement thresholds in ZnO, IEEE Transactions on Nuclear Science 19 (6) (1972) 237–242. doi:10.1109/tns.1972.4326839.

[263] T. Yoshiie, H. Iwanaga, N. Shibata, M. Ichihara, S. Takeuchi, Orientation dependence of electron-irradiation damage in zinc oxide, Philosophical Magazine A 40 (2) (1979) 297–301. doi:10.1080/01418617908243104.

[264] D. C. Look, G. C. Farlow, P. Reunchan, S. Limpijumnong, S. B. Zhang, K. Nordlund, Evidence for native-defect donors in n-type ZnO, Physical Review Letters 95 (22) (2005) 225502. doi:10.1103/physrevlett.95.225502.

[265] K. E. Knutsen, A. Galeckas, A. Zubiaga, F. Tuomisto, G. C. Farlow, B. G. Svensson, A. Y. Kuznetsov, Zinc vacancy and oxygen interstitial in ZnO revealed by sequential annealing and electron irradiation, Physical Review B 86 (12) (2012) 121203. doi:10.1103/physrevb.86.121203.

[266] Y. Chen, F. Meng, F. Ge, F. Huang, Ga-doped ZnO films by magnetron sputtering at ultralow discharge voltages: effects of defect annihilation, Thin Solid Films 644 (2017) 16–22. doi:10.1016/j.tsf.2017.05.055.

[267] G. Bizarri, B. Moine, On $BaMgAl_{10}O_{17}$:Eu^{2+} phosphor degradation mechanism by vacuum-ultraviolet excitation, Journal of Applied Physics 98 (11) (2005) 113528. doi:10.1063/1.2132094.

[268] E. Takeda, T. Zukawa, T. Ishibashi, K. Yoshino, Y. Morita, M. Fujii, Mechanisms for the degradation of phosphor excitation efficiency by short wavelength vacuum ultraviolet radiation in plasma discharge devices, Journal of Physics and Chemistry of Solids 124 (2019) 274–280. doi:10.1016/j.jpcs.2018.08.033.

[269] M. Uchidoi, Critical aspects of the plasma display panel manufacturing process, IEEE Transactions on Plasma Science 34 (2) (2006) 287–293. doi:10.1109/tps.2006.872437.

[270] L. F. Weber, History of the plasma display panel, IEEE Transactions on Plasma Science 34 (2) (2006) 268–278. doi:10.1109/tps.2006.872440.

[271] E. Chason, M. Karlson, J. Colin, D. Magnfält, K. Sarakinos, G. Abadias, A kinetic model for stress generation in thin films grown from energetic vapor fluxes, Journal

of Applied Physics 119 (14) (2016) 145307. doi:10.1063/1.4946039.

[272] P. F. P. F. Carcia, R. S. McLean, M. H. Reilly, Z. G. Li, L. J. Pillione, R. F. Messier, Low-stress indium-tin-oxide thin films rf magnetron sputtered on polyester substrates, Applied Physics Letters 81 (10) (2002) 1800–1802. doi:10.1063/1.1504874.

[273] M. R. Davidson, B. Pathangey, P. H. Holloway, P. D. Rack, S. S. Sun, C. N. King, Sputter deposition of phosphors for electroluminescent flat panel displays, Journal of Electronic Materials 26 (11) (1997) 1355–1360. doi:10.1007/s11664-997-0084-x.

[274] D. R. Lide, CRC Handbook of chemistry and physics, CRC-Press, 1997.

[275] K. Ellmer, R. Mientus, S. Seeger, V. Weiß, Highly (001)-textured $WS_{2\text{-}x}$ films prepared by reactive radio frequency magnetron sputtering, physica status solidi (a) 201 (14) (2004) R97–R100. doi:10.1002/pssa.200409067.

[276] K. Ellmer, S. Seeger, I. Sieber, W. Bohne, J. Röhrich, E. Strub, R. Mientus, Reactive magnetron sputtering of highly (001)-textured $WS_{2\text{-}x}$ films: Influence of Ne^+, $Ar^+$and Xe^+ ion bombardment on the film growth, physica status solidi (a) 203 (3) (2006) 497–503. doi:10.1002/pssa.200521363.

[277] V. Weiß, S. Seeger, K. Ellmer, R. Mientus, Reactive magnetron sputtering of tungsten disulfide ($WS_{2\text{-}x}$) films: Influence of deposition parameters on texture, microstructure, and stoichiometry, Journal of Applied Physics 101 (10) (2007) 103502. doi:10.1063/1.2716395.

[278] K. Ellmer, Preparation routes based on magnetron sputtering for tungsten disulfide (WS_2) films for thin-film solar cells, physica status solidi (b) 245 (9) (2008) 1745–1760. doi:10.1002/pssb.200879545.

[279] V. Weiß, W. W. Bohne, J. Röhrich, E. Strub, U. Bloeck, I. Sieber, K. Ellmer, R. Mientus, F. Porsch, Reactive magnetron sputtering of molybdenum sulfide thin films: in-situ synchrotron x-ray diffraction and transmission electron microscopy study, Journal of Applied Physics 95 (12) (2004) 7665–7673. doi:10.1063/1.1736323.

[280] T. Unold, I. Sieber, K. Ellmer, Efficient $CuInS_2$ solar cells by reactive magnetron sputtering, Applied Physics Letters 88 (21) (2006) 213502. doi:10.1063/1.2205756.

[281] S. Seeger, K. Harbauer, K. Ellmer, Ion-energy distributions at a substrate in reactive magnetron sputtering discharges in Ar/H_2S from copper, indium, and tungsten targets, Journal of Applied Physics 105 (5) (2009) 053305. doi:10.1063/1.3086618.

[282] T. Tominaga, S. Takayanagi, T. Yanagitani, Negative-ion bombardment increases during low-pressure sputtering deposition and their effects on the crystallinaties and piezoelectric properties of scandium aluminum nitride films, J. Phys. D.: Appl. Phys. 55 (2022) 105306. doi:10.1088/1361-6463/ac3d5c.